EFFICIENT PHOTON PAIR GENERATION FOR QUANTUM INFORMATION TECHNOLOGIES

A Thesis Submitted to
the Graduate School of
İzmir Institute of Technology
in Partial Fulfillment of the Requirements for the Degree of

MASTER OF SCIENCE

in Physics

by
Furkan AĞLARCI

July 2024
İZMİR

We approve the thesis of **Furkan AĞLARCI**

Examining Committee Members:

Assoc. Prof. Serkan ATEŞ
Department of Physics, İzmir Institute of Technology

Assoc. Prof. Özür ÇAKIR
Department of Physics, İzmir Institute of Technology

Prof. Dr. Göktuğ KARPAT
Department of Physics, İzmir University of Economics

10 July 2024

Assoc. Prof. Serkan ATEŞ
Supervisor, Department of Physics
İzmir Institute of Technology

Prof. Dr. Lütfi ÖZYÜZER
Head of the Department of Physics

Prof. Dr. Mehtap EANES
Dean of the Graduate School

ABSTRACT

EFFICIENT PHOTON PAIR GENERATION FOR QUANTUM INFORMATION TECHNOLOGIES

This thesis focuses on the design parameters of waveguides and ring resonators to generate photon pairs through the four-wave mixing process. The goal was to design these components specifically for generating visible-range photon pairs with the intention of using visible-range photodetectors. These detectors offer a better photon detection range, lower dark count, and faster response time compared to their telecom-range counterparts. Additionally, visible wavelength photons are more effective in free-space communication.

A photonic platform, such as a Si_3N_4 waveguide or a ring resonator on a SiO_2 layer, is utilized for photon pair generation due to several advantages. These advantages include the ability to leverage CMOS technologies and operate at room temperature. The choice of Si_3N_4 material aims to avoid a two-photon absorption process. Compared to Si-based sources, which exhibit a two-photon absorption process due to their band energy, utilizing Si_3N_4 helps circumvent this issue.

In this thesis, the dimensions of the waveguide are tailored to satisfy the phase-matching condition, and its dispersion properties are studied. A ring resonator is constructed based on determined dimensions, and its spectral characteristics are analyzed for efficient photon pair generation.

ÖZET

KUANTUM BİLİŞİM TEKNOLOJİLERİ İÇİN VERİMLİ FOTON ÇİFTİ ÜRETİMİ

Bu tez, dört dalga karışım (FWM) süreci yoluyla görünür dalga boylarında foton çiftleri üretmek için kullanılan dalga kılavuzu ve halka rezonatörün tasarım parametrelerine odaklanmaktadır. Tezin amacı, görünür dalga boylarında foton çiftleri üretmektir ve bu fotonları algılamak için görünür dalga boyunda çalışan fotodedektörler kullanılmaktadır. Bu dedektörler, telekomünikasyon muadillerine kıyasla daha iyi foton algılama aralıgı, daha düşük karanlık sayım ve hızlı tepki süresi sunmaktadır. Ayrıca, görünür dalga boyundaki fotonlar serbest uzay iletişiminde daha etkilidir.

Foton çift üretimi için $\mathrm{Si_3N_4}$ dalga kılavuzu veya $\mathrm{SiO_2}$ tabakası üzerindeki halka rezonatör gibi bir fotonik platform tercih edilmektedir. Bu platformlar, CMOS teknolojilerini kullanma ve oda sıcaklıgında çalışma gibi avantajlar sağlar. $\mathrm{Si_3N_4}$ malzemesinin tercih edilme nedeni, iki foton emilim sürecinden kaçınmaktır. Si bazlı kaynaklar, bant enerjileri nedeniyle iki foton emilim süreci sergilerken, $\mathrm{Si_3N_4}$ kullanımı bu sorunu ortadan kaldırır.

Tezde, dalga kılavuzunun boyutları faz uyumu koşulunu sağlamak amacıyla tasarlanmış ve dispersiyon özellikleri incelenmiştir. Belirlenen boyutlara göre tasarlanan halka rezonatör, spektral özellikleri açısından verimli foton çift üretimi için analiz edilmiştir.

TABLE OF CONTENTS

LIST OF FIGURES

LIST OF TABLES

CHAPTER 1

INTRODUCTION

Photon pair sources form the foundation of quantum communication[2] and quantum information processes[3], including quantum cryptography, quantum computing, and quantum teleportation. Consequently, photonic quantum technologies[4] have become an extensively studied area due to their advantages, such as the scalability and integrability of quantum applications. Besides, they benefit from a technological background of CMOS technologies for production, making them cost-effective and reliable and providing the possibility of mass production. Moreover, they provide easy integration into fiber networks, especially in the telecom band. Recent studies have shown that integrated platforms with high spectral brightness, photon purity, and long coherence time at room temperature are promising for generating photon pairs in the telecommunications band. However, these photon pair sources are not efficiently compatible with the current photodetector. Most visible-range photodetectors, such as silicon avalanche photodetectors, offer higher photon detection rates and lower dark counts than their infrared counterparts. Besides, this detector response time is quite high for correlation measurement. All these advantages of visible range photodetectors contribute to reducing noise, increasing fidelity, detecting weak signals, and providing higher resolution. Moreover, visible-range photon pairs are better for free-space communication. Thus, it urges us to study visible range photon pair generation on photonic platforms. On the other hand, it has been shown that generating visible-telecom entangled photon pair in Si_3N_4 ring resonator is possible[5]. It motivates the combination of quantum memories that operate in the visible range and telecommunication networks.

1.1. Thesis Outline

The thesis focuses on numerically studying waveguide and microring resonator structures to generate photon pairs using Si_3N_4 material at the visible spectrum edge. Chapter 2 provides a basic overview of the formulation of nonlinear optical processes, including sum frequency generation and Four-wave mixing (FWM) processes. The chapter then discusses the phase-matching requirement for the FWM process in the context of dispersion regimes for waveguides. Additionally, the material's susceptibilities are examined within the framework of quantum mechanical description for nonlinear optical processes.

In Chapter 3, commonly used waveguide structures are introduced, followed by a discussion of materials used in the literature for various applications in nonlinear optics. The chapter then demonstrates dispersion engineering to meet the phase requirement necessary for the FWM process. It emphasizes that tailoring the material geometry can change waveguide properties such as group velocity, dispersion, and effective refractive index. It is also shown that proper waveguide dimensions can be determined through numerical investigation, serving as the basis for the design of the ring resonator.

Chapter 4 provides a detailed simulation result of a ring resonator, explaining how the cavity mode amplifies the nonlinear interaction, leading to a significant improvement in the efficiency of photon pair generation.

CHAPTER 2

NONLINEAR OPTICS

Nonlinear optics is a field of study that examines the interaction between light and matter, specifically focusing on the effects that alter in a nonlinear manner. This means that, when exposed to incident light, a material's optical properties undergo changes. The material's response depends on the intensity of the incident light, and it is said that, due to their high power, only lasers can unveil the nonlinear characteristics of materials. To clarify the nonlinear effect, polarization is defined as the dipole moment per volume. This refers to the phenomenon where the electric field of incident light causes a bounded electron cloud to move in a dielectric substance, resulting in the separation of charges that constitute dipoles. These dipoles align inside the material because of an external field, leading to a net polarization effect. Nonetheless, some materials have already inherited polarization properties, meaning that the source of polarization is not an external field. The polarization of the material is conventionally linearly proportional to the electric field strength of the incident light, i.e., $P(t) = \epsilon_0 \chi^{(1)} E(t)$. However, this statement ceases to be true under the influence of high-power light. Generally, polarization is expressed in a power series of electric field strength in nonlinear optics.

$$P(t) = \epsilon_0 (\chi^{(1)} E(t) + \chi^{(2)} E^2(t) + \chi^{(3)} E^3(t) + \cdots) \tag{2.1}$$

where $\chi^{(2)}, \chi^{(3)}$ are the second and third order nonlinear susceptibilities and ϵ_0 is free space permittivity. It is assumed that time-dependent polarization relies on the electric field instantaneously, implying that the light does not experience any loss or dispersion in the material. The fact that time-varying polarization can result in the generation of new electromagnetic field components. In other words, new frequency components can be created from incident electromagnetic fields due to nonlinear interactions. To see this generation in the context of Maxwell's equations, the wave equation for source, current-free, and nonmagnetic medium is described by

$$\nabla^2 \boldsymbol{E} - \frac{1}{c^2} \frac{\partial^2 \boldsymbol{E}}{\partial t^2} = \frac{1}{\epsilon_0 c^2} \frac{\partial^2 \boldsymbol{P}}{\partial t^2} \tag{2.2}$$

where c is the speed of light in a vacuum and n is the refractive index. wave equation can be described in terms of electric displacement field $\boldsymbol{D}$, where

$$\boldsymbol{D} = \epsilon_0 \boldsymbol{E} + \boldsymbol{P} \tag{2.3}$$

and the wave equation becomes

$$\nabla^2 \boldsymbol{E} - \frac{1}{\epsilon_0 c^2} \frac{\partial^2 \boldsymbol{D}}{\partial t^2} = 0 \tag{2.4}$$

The displacement field is the result of the combination of the external electric fields and the electric fields generated by the dipoles present in the material. One may separate the polarization and displacement fields into linear and nonlinear components.

$$\boldsymbol{P} = \boldsymbol{P}^{(1)} + \boldsymbol{P}^{NL} \tag{2.5a}$$

$$\boldsymbol{D} = \boldsymbol{D}^{(1)} + \boldsymbol{P}^{NL} \tag{2.5b}$$

$\boldsymbol{P}^{(1)}$ and $\boldsymbol{D}^{(1)}$ are linear terms and $\boldsymbol{D}^{(1)}$ can be written as

$$\boldsymbol{D}^{(1)} = \epsilon_0 \boldsymbol{E} + \boldsymbol{P}^{(1)} \tag{2.6}$$

Equation (2.2) has the form using equations (2.5) and (2.6)

$$\nabla^2 \boldsymbol{E} - \frac{1}{\epsilon_0 c^2} \frac{\partial^2 \boldsymbol{D}^{(1)}}{\partial t^2} = \frac{1}{\epsilon_0 c^2} \frac{\partial^2 \boldsymbol{P}^{NL}}{\partial t^2} \tag{2.7}$$

This form of the inhomogeneous wave equation in equation (2.7) makes it easier to use a dielectric tensor, which is important in understanding how light interacts with matter and characterizing material anisotropy. This involves determining the principal refractive indexes and the corresponding optical axes. Furthermore, the material's nonlinear response, which appears on the right-hand side of the equation, acts as a source of new electromagnetic field components. To derive the general expression of the wave equation, fields are written as the sum of their frequency components

$$\boldsymbol{E}(\boldsymbol{r}, t) = \textstyle\sum_n \boldsymbol{E}_n(r) e^{-i\omega_n t} + c.c \tag{2.8a}$$

$$\boldsymbol{D}^{(1)}(\boldsymbol{r}, t) = \textstyle\sum_n \boldsymbol{D}_n^{(1)}(r) e^{-i\omega_n t} + c.c \tag{2.8b}$$

$$\boldsymbol{P}^{NL}(\boldsymbol{r}, t) = \textstyle\sum_n \boldsymbol{P}_n^{NL}(r) e^{-i\omega_n t} + c.c \tag{2.8c}$$

The first-order frequency-depended displacement field can be written as in equation (2.9) where the relation comes from $\boldsymbol{D} = \epsilon_0 \boldsymbol{E} + \epsilon_0 \chi^{(1)\boldsymbol{E}} = \epsilon_0(1 + \chi^{(1)})\boldsymbol{E} = \epsilon \boldsymbol{E}$. ϵ is called permittivity of the material describing how easily dielectric material can be polarized as in that χ. ϵ does not need to be scalar; it can be treated as a tensor. It is critical to use as a tensor, especially in anisotropic material where the charges readily move along particular axes. Besides, in anisotropic materials, the directions of the external fields and the polarization are not the same.

$$\boldsymbol{D}_n^{(1)}(\boldsymbol{r}) = \epsilon_0 \boldsymbol{\epsilon}^{(1)}(\omega_n) \cdot \boldsymbol{E}_n(\boldsymbol{r}) \tag{2.9}$$

Substituting the equations (2.8) and (2.9) into equation (2.7) yields

$$\nabla^2 \boldsymbol{E}_n(\boldsymbol{r}) + \frac{\omega_n^2}{c^2} \boldsymbol{\epsilon}^{(1)}(\omega_n) \cdot \boldsymbol{E}_n(\boldsymbol{r}) = -\frac{\omega_n^2}{\epsilon_0 c^2} \boldsymbol{P}_n^{NL}(\boldsymbol{r}) \tag{2.10}$$

Equation (2.10) is known as the Helmholtz equation in the frequency domain.

2.1. Nonlinear Optical Processes

The polarization of materials related to crystal symmetry is crucial in determining the type of nonlinear optical processes. Second-order nonlinear interaction takes place in non-centrosymmetric materials such as $LiNbO_3$ and KTP. Centrosymmetry, also known as inversion symmetry, means the material remains unchanged when the coordinates are inverted through its center. The material must lack inversion symmetry to observe the $\chi^{(2)}$ response. On the other hand, the $\chi^{(3)}$ response can be observed in both isotropic and anisotropic mediums. In an isotropic medium, the material properties remain the same in all directions, resulting in $\chi^{(3)}$ being simplified to a scalar quantity. This causes the material to be unaffected by the polarization of the applied field. Only changes in the refractive index occur due to the Kerr effect (discussed in section (2.1.2.3)), which is also independent of the polarization of the applied field. For an anisotropic medium, the third-order nonlinear susceptibility ($\chi^{(3)}$) becomes a tensor quantity, and the third-order nonlinear response varies depending on the polarization of the applied field. This polarization dependence is also important to consider for phase matching in the FWM process. However, in this thesis, the study focuses on Si_3N_4, which is a typically isotropic material. The polarization of the input field in the ring resonator simulation is chosen to ensure efficient coupling from the bus waveguide to the ring resonator. Figure (2.1) illustrates the time-dependent polarization response of $\chi^{(2)}$ and $\chi^{(3)}$ materials. The following section discusses the related nonlinear optical processes of these materials, specifically sum-frequency generation and four-wave mixing.

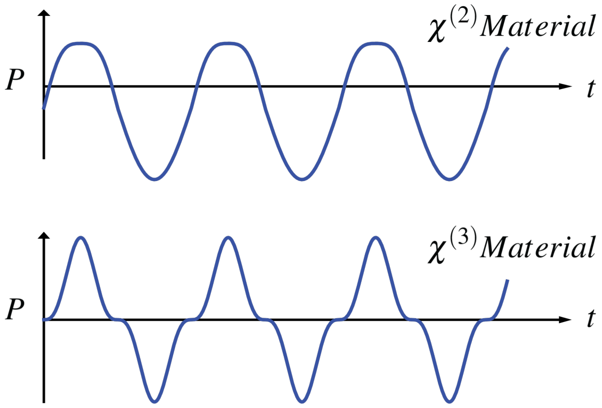

Figure 2.1. Polarization as a functions of time of $\chi^{(2)}$, and $\chi^{(3)}$ materials

2.1.1. Sum-Frequency Generation

Sum-frequency generation can be considered as an instance of second-order nonlinear interaction in which the frequencies of the input fields are denoted as ω_1 and ω_2, and the frequency of the output field is ω_3. Due to the applied electric field, the atoms within the nonlinear material undergo oscillations. The oscillation of the electron cloud can result in the emission of dipole radiation. Nevertheless, the incident field determines whether the dipole emission contains the frequencies of $\omega_3 = \omega_1 + \omega_2$. If the dipole emissions are in phase, they will combine constructively, leading to the emission of radiation in a beam form from the material. It is said that the phase-matching condition is satisfied.

The frequency components of the input fields are expressed as follows:

$$E_j(z,t) = E_j e^{-i\omega_j t} + c.c, \quad E_j = A_i e^{ik_j z}, \quad j = 1,2 \tag{2.11}$$

and using equation (2.1), second order term of the polarization is given as

$$P^{(2)}(t) = \epsilon_0 \chi^{(2)} E(t)^2 \tag{2.12}$$

substituting the input fields equations (2.11) into the second-order polarization equation (2.12) gives rise

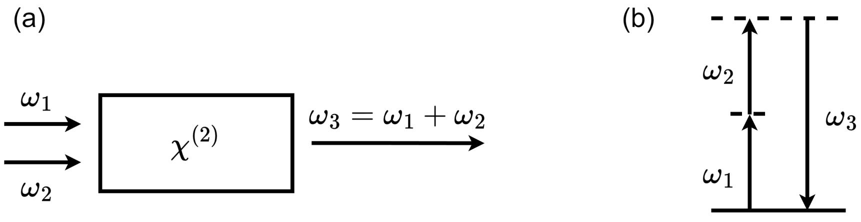

Figure 2.2. a) Geometric representation of sum frequency generation. b) Energy level diagram of sum frequency generation

$$\begin{aligned} P^{(2)}(t) =& \epsilon_0 \chi^{(2)} [E_1^2 e^{-2i\omega_1 t} + E_2^2 e^{-2i\omega_2 t} + 2E_1 E_2 e^{-i(\omega_1+\omega_2)t} \\ &+ 2E_1 E_2^* e^{-i(\omega_1-\omega_2)t} + c.c] + 2\epsilon_0 \chi^{(2)} [E_1 E_1^* + E_2 E_2^*] \end{aligned} \tag{2.13}$$

Considering each component separately,

$$P(2\omega_1) = \epsilon_0 \chi^{(2)} E_1^2 \tag{2.14a}$$

$$P(2\omega_2) = 2\epsilon_0 \chi^{(2)} E_2^2 \tag{2.14b}$$

$$P(\omega_1 + \omega_2) = 2\epsilon_0 \chi^{(2)} E_1 E_2 \tag{2.14c}$$

$$P(\omega_1 - \omega_2) = 2\epsilon_0 \chi^{(2)} E_1 E_2^* \tag{2.14d}$$

$$P(0) = 2\epsilon_0 \chi^{(2)} (E_1 E_1^* + E_2 E_2^*) \tag{2.14e}$$

they show second-order interactions, equation (2.14a) through (2.14e) indicates second harmonic generations (SHG) with different frequencies, sum-frequency generation (SFG), difference-frequency generation (DFG), and optical rectification (OR) respectively. In order to confirm the validity of sum-frequency generation, each frequency component of the field must fulfill equation (2.10). A comprehensive understanding of nonlinear interactions requires a thorough knowledge of polarization. Generally, while taking into account the tensor properties of permittivity, polarization is represented by

$$P_i(\omega_i + \omega_j) = \epsilon \sum_{jk} \sum_{(nm)} \chi_{ijk}^{(2)} (\omega_n + \omega_m, \omega_n, \omega_m) E_j(\omega_n) E_k(\omega_m) \tag{2.15}$$

Summation is performed overall positive and negative frequency components for all directions; thus, certain circumstances must be considered. Since polarization is a measurable quantity, it must conform to conditions

$$P_i(-\omega_n - \omega_m) = P_i(\omega_n + \omega_m)^* \tag{2.16}$$

A similar fashion happens for complex frequency components of electric fields.

$$E_j = (-\omega_n) = E_j(\omega_n)^* \tag{2.17a}$$

$$E_k = (-\omega_m) = E_k(\omega_m)^* \tag{2.17b}$$

The relation between polarization and susceptibility indicates

$$\chi^{(2)}_{ijk}(-\omega_n - \omega_m, -\omega_n, -\omega_m) = \chi^{(2)}_{ijk}(\omega_n + \omega_m, \omega_n, \omega_m)^* \tag{2.18}$$

The susceptibility tensor can be reduced due to symmetries such as full permutation symmetry, which is related to the interchangeability of the frequency component of nonlinear susceptibility. Each frequency component of the susceptibility tensor can be changed if the corresponding Cartesian coordinate indices change in the correct order. If the medium has a considerable optical loss, then the product of field components can only be interchanged, such as $E_j(\omega_n)E_k(\omega_m)$.

Furthermore, The optical properties of the medium are related to the arrangement of the atoms and ions in the crystal. Symmetrical medium refers to these properties that remain invariant under transformation, such as reflection, rotation, and translation. In nonlinear optics, symmetry is crucial in determining the behavior of the light-matter interaction. In some cases, the material exhibits spatial and inversion symmetry, which is the scope of Kleinman's symmetry. Kleinman's symmetry is based on the concept that the nonlinear polarization response of a crystal is influenced by the input and output polarization states, as well as the symmetry of the crystal lattice. By analyzing the symmetry features of the crystal and the polarization states of the input and output, it is possible to analyze the connections between the components of the nonlinear susceptibility tensor and can reduce the number of independent variables in the tensor. It is quite helpful to identify and simplify relationships between the tensor's elements, and it is a powerful tool for designing optical devices; however, Kleiman symmetry conditions are valid where the medium is dispersionless.

To capture the material's complete nonlinear response, frequency components of polarization must satisfy the equation (2.10); the nonlinear source term $\boldsymbol{P}_n^{NL}(\boldsymbol{r})$ that appears in the equation (2.10) is indicated as

$$P_3(z,t) = P_3 e^{i\omega_3 t} + c.c \tag{2.19}$$

assuming fields are linearly polarized, and propagation direction is $\hat{z}$. According to equation (2.15),

$$P_3 = 4\epsilon_0 d_{eff} E_1 E_2 \tag{2.20}$$

where $d_{ijk} = \frac{1}{2}\chi_{ijk}^{(2)}$ and the effective value of the d_{eff} is the calculated value that considers the crystal orientation, frequency of incident light, and symmetry properties of the material. Finding the strength is crucial to revealing nonlinear effects.

Substituting the input fields that are defined in equation (2.11) into equation (2.20) yields amplitude of the nonlinear polarization of P_3

$$P_3 = 4\epsilon_0 d_{eff} A_1 A_2 e^{i(k_1+k_2)z} = p_3 e^{i(k1+k2)z} \tag{2.21}$$

Following the second-order interaction, it is anticipated that the solution of equation (2.10) for generating the electromagnetic field at ω_3 will be a plane wave propagating in $\hat{z}$ direction. Put simply, when the wave equation lacks a nonlinear source element, the solution takes the form of a plane wave at ω_3 as

$$E_3(z,t) = A_3 e^{i(kz-\omega t)} + c.c \tag{2.22}$$

It is assumed that A_3 is a slowly varying amplitude function in the propagation direction and can be regarded as constant.

By transforming the right-hand side of the equation (2.10) into an appropriate form, one can demonstrate the interaction between two fields in a nonlinear medium resulting in the emergence of a new field. Substituting equations (2.11), (2.21) and (2.22) into equation (2.10) obtains

$$\frac{d^2 A_3}{dz^2} + 2ik_3\frac{dA_3}{dz} = \frac{-4d_{\text{eff}}\omega_3^2}{c^2} A_1 A_2 e^{i(k_1+k_2-k_3)z} \tag{2.23}$$

cancellation occurs since $k_3^2 = \epsilon^{(1)}(\omega_3)\omega_3^2/c^2$ and the first term is comparatively smaller than the second term on the left side of the equation as

$$\left|\frac{d^2 A_3}{dz^2}\right| \ll \left|k_3\frac{d^2 A_3}{dz}\right| \tag{2.24}$$

This is known as slowly varying amplitude approximation. Equation (2.23) becomes, while taking $k_3 = \omega_3 n_3 / c$

$$\frac{dA_3}{dz} = \frac{2id_{eff}\omega_3}{n_3 c} A_1 A_2 e^{i\Delta kz} \tag{2.25}$$

where n_3 is the refractive index of material for the field at ω_3, and it is assumed that amplitudes A_1, A_2 do not vary, so they can be taken as constant. This equation is called coupled-amplitude equation, which indicates how much amplitude of the ω_3 field is generated due to coupling of ω_1 and ω_2 fields. The momentum mismatch is defined as

$$\Delta k = k_1 + k_2 - k_3 \tag{2.26}$$

Perfect phase matching condition is satisfied where

$$\Delta k = 0 \tag{2.27}$$

If this condition is satisfied, the output wave at ω_3 is efficiently generated from incident waves. In other words, emissions from each dipole in the material are coherently added, resulting in an output wave in the propagation direction.

2.1.2. Four Wave Mixing

FWM is a nonlinear process that generates two output field waves as a result of third-order interaction. In FWM, two input fields with frequencies ω_1 and ω_2 lead to the generation of output fields with frequencies ω_3 and ω_4 as a result of the interaction of these four waves inside the nonlinear material. Even though FWM has two output fields and third-order interaction, the first analytical viewpoint closely resembles sum-frequency generation. Initially, fields and polarization are defined and inserted into the wave equation. Subsequently, the solution of the coupled wave equation reveals the prerequisites for the generation of new waves.

Polarization, in general, impacts the FWM process. In this study, the scalar case of the FWM theory is examined, where all the fields' polarizations are aligned along the same axis and propagation direction is $\hat{z}$; thus, the total electric field is described by

$$\boldsymbol{E} = \frac{1}{2}\sum_{j=1}^{4} E_j e^{i(\beta_j z - \omega_j t)} + c.c \tag{2.28}$$

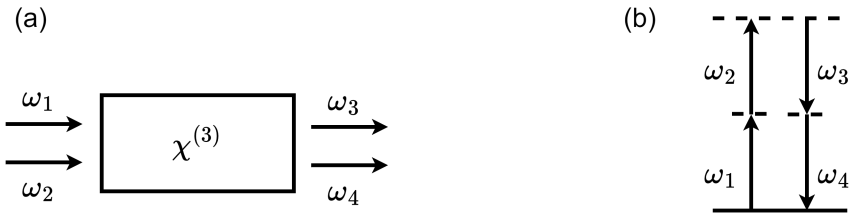

Figure 2.3. a) Geometric representation of four-wave mixing. b) Energy level diagram of four-wave mixing

where β is defined as propagation constant;

$$\beta = \frac{n(\omega)\omega}{c} \tag{2.29}$$

here n indicates the mode index. Analogously, the nonlinear source term is defined as

$$\boldsymbol{P}^{NL} = \frac{1}{2}\sum_{j=1}^{4} P_j e^{i(\beta_j z - \omega_j t)} + c.c \tag{2.30}$$

The 1/2 term appears before the total electric fields and polarizations to avoid double counting when considering intensity calculations. From equation (2.1), third-order polarization is written as

$$P(t) = \epsilon_0 \chi^{(3)} E^3(t) \tag{2.31}$$

Substituting equation (2.28) into equation (2.31) reveals many interaction terms due to products of electric fields. One of them is P_4 which is found as

$$\begin{aligned} P_4 =& \frac{3\epsilon_0}{4}\chi^{(3)}_{xxxx}[|E_4|^2 E_4 + 2(|E_1|^2 + |E_2|^2 + |E_3|^2)E_4 \\ &+ 2E_1E_2E_3e^{i\theta_+} + 2E_1E_2E_3^{*}e^{i\theta_-} + \dots] \end{aligned} \tag{2.32}$$

where

$$\theta_+ = (\beta_1 + \beta_2 + \beta_3 - \beta_4)z - (\omega_1 + \omega_2 + \omega_3 - \omega_4)t \tag{2.33a}$$

$$\theta_- = (\beta_1 + \beta_2 - \beta_3 - \beta_4)z - (\omega_1 + \omega_2 - \omega_3 - \omega_4)t \tag{2.33b}$$

Equations (2.33a) and (2.33b) classify the type of FWM process in a certain way if the phase matching condition is satisfied, such as θ_+, which is responsible for the generation of a single frequency field at ω_4 from the interaction of three different frequency fields at ω_1, ω_2 and ω_3 i.e., $\omega_4 = \omega_1 + \omega_2 + \omega_3$. If $\omega_1 = \omega_2 = \omega_3$, then the process is called third-harmonic generation. On the other hand, θ_- is accountable for generating two new frequency fields from two different incident frequency fields where

$$\omega_3 + \omega_4 = \omega_1 + \omega_2 \tag{2.34a}$$

$$\beta_3 + \beta_4 = \beta_1 + \beta_2 \tag{2.34b}$$

It is considered a general case for FWM to occur where $\omega_1 \neq \omega_2$. Nonetheless, we are quite interested in a special case where $\omega_1 = \omega_2$, in other words, a degenerate case. In this special case, only one strong pump laser can lead to the generation of two new frequency fields. From the point of view of quantum mechanics, when the conditions for energy (2.34a) and momentum (2.34b) conservation are satisfied, two photons with the same energy are destroyed, and two photons with a different frequency are created simultaneously in the nonlinear matter. A high-power laser pump at frequency ω_1 generates two sidebands at frequencies ω_3 and ω_4, which are symmetrically positioned relative to ω_1. The frequency shift is given by

$$\Omega = \omega_1 - \omega_3 = \omega_4 - \omega_1 \tag{2.35}$$

assuming $\omega_3 < \omega_4$. Pump frequency $\omega_{1,2}$ can also be represented as ω_p. Additionally, ω_3 can written as ω_s, whereas ω_4 can be written as ω_i, which denotes the Stokes and anti-Stokes bands of ω_p, respectively. The Stokes band corresponds to lower energy, while the anti-Stokes band corresponds to higher energy. Generally, the Stokes band refers to the signal wave, whereas the anti-Stokes band refers to the idler wave. This process is shown in Figure (2.4), where a single pump field interacts with a $\chi^{(3)}$ material, resulting in the generation of the signal and idler waves from the noise.

On the other hand, the common case is pump degenerate FWM, where the weak signal wave participates in the interaction, leading to the amplification of the signal wave and generation of the idler wave simultaneously. This kind of amplification being referred to is known as parametric gain, and energy conservation for pump degenerate FWM becomes $\omega_i = 2\omega_p - \omega_s$. This process is illustrated in Figure (2.5)

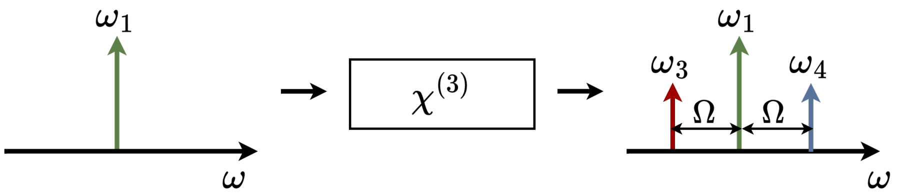

Figure 2.4. Representation of generated signal and idler waves using FWM with a single pump field.

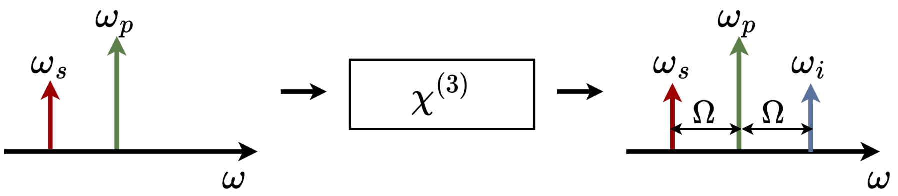

Figure 2.5. Representation of signal and idler waves using FWM with pump degenerate field

One must solve the wave equation to describe the interaction between the pump, signal, and idler waves. A similar methodology is used as previously: putting electric fields and both linear and nonlinear polarization terms in the wave equation yields coupled differential equations. It is necessary to consider the spatial distribution and spatial symmetries inside the nonlinear material, namely the silicon nitride waveguide discussed in this thesis. One may spatial distribution $F(x, y)$ can be inserted in the electric field such as $E_j(\boldsymbol{r}) = F_j(x, y)A_j(z)$. Spatial distribution defines how much field is distributed over the material. Considering the waveguide, it shows how much field is confined. Additionally, it establishes the amplitude profile on the cross-section of the waveguide on the x, y plane, which is expected to be the same during propagation. Spatial distribution is also related to the overlap integral, which defines spatial overlap between the fields inside the material. This plays a crucial role in nonlinear interaction because it identifies how much overlap occurs between pump, signal, and idler waves. Besides, if the overlap is robust, interaction is said to be efficient. Understanding the relationship between spatial distribution and waveguide geometry allows efficient optical systems engineering.The overlap integral f_{ijkl} is given by

$$f_{ijkl} = \frac{\langle F_i^* F_j^* F_k F_l \rangle}{[\langle |F_i|^2 \rangle \langle |F_j|^2 \rangle \langle |F_k|^2 \rangle \langle |F_l|^2 \rangle]^{1/2}} \tag{2.36}$$

where $\langle\rangle$ indicates the integration over x and y coordinates. Assuming pump laser intensity high enough (much stronger than signal and idler) and undepleted, then overlap integral can be approximated as

$$f_{ijkl} \approx f_{ij} \approx \frac{1}{A_{eff}} \tag{2.37}$$

where A_{eff} is the effective mode area (discussed in section (3.4)) of the single-mode waveguide. Thus, the coupled differential equation for pump, signal, and idler fields can be written as:

$$\frac{dE_p}{dz} = i\gamma \left[\left(|E_p|^2 + 2(|E_s|^2 + |E_i|^2) \right) E_p + 2E_s E_i E_p^* e^{(i\Delta\beta z)} \right] \tag{2.38a}$$

$$\frac{dE_s}{dz} = i\gamma \left[\left(|E_s|^2 + 2(|E_p|^2 + |E_i|^2) \right) E_s + E_i^* E_p^2 e^{(-i\Delta\beta z)} \right] \tag{2.38b}$$

$$\frac{dE_i}{dz} = i\gamma \left[\left(|E_i|^2 + 2(|E_p|^2 + |E_s|^2) \right) E_i + E_s^* E_p^2 e^{(-i\Delta\beta z)} \right] \tag{2.38c}$$

It is assumed that all the polarization and overlap are the same. The nonlinear parameter that appears in coupled differential equations is defined by

$$\gamma \approx \frac{n_2 \omega_j}{c A_{eff}} \tag{2.39}$$

where n_2 is the Kerr index (detail in section (2.1.2.3)) or nonlinear index coefficient, which has information about $\chi^{(3)}$ interaction and field confinement, whereas mismatch of propagation constant is

$$\Delta\beta = 2\beta_p - \beta_s - \beta_i \tag{2.40}$$

β_p, β_s, and β_i are propagation constants of pump, signal, and idler fields.

2.1.2.1. Phase Matching

To achieve an efficient FWM process, it is necessary to ensure that momentum conservation is satisfied. The Solution of the couple differential equation results in a criterion known as effective phase mismatch that is slightly different than the phase matching requirement $\Delta k = 0$ for sum-frequency generation, and it is defined as

$$\kappa \equiv \Delta\beta + 2\gamma P_p = 0 \tag{2.41}$$

The effective phase mismatch quantifies the degree of efficiency in converting the interacting waves. It also includes an additional γP_p term to account for the phase shift caused by the Kerr effect. The coefficient of 2 in the equation (2.41) is included for degenerate FWM. To fulfill the phase-matching condition in the equation (2.41), some terms must be negative. Regarding this matter, κ can be separated as

$$\kappa = \underbrace{\Delta k_M + \Delta k_W}_{\Delta\beta} + \underbrace{\Delta k_{NL}}_{2\gamma P} = 0 \tag{2.42}$$

where Δk_M, Δ_W, and Δ_{NL} are phase mismatches due to material dispersion, waveguide dispersion, and nonlinear effect, respectively. Regarding the effective indices as

$$n_{eff} = n_M(\omega) + \Delta n \tag{2.43}$$

Equation (2.43) indicates propagating fields experience changing refractive index due to waveguiding, and this additional term is written as Δn. Considering the degenerate FWM phase mismatches can be written as

$$\begin{aligned} \Delta k_M &= (n_3\omega_3 + n_4\omega_4 - 2n_1\omega_1)/c && \text{(2.44a)} \\ \Delta k_W &= (\Delta n_3\omega_3 + \Delta n_4\omega_4 - (\Delta n_1 + \Delta n_2)\omega_1)/c && \text{(2.44b)} \\ \Delta k_{NL} &= 2\gamma P && \text{(2.44c)} \end{aligned}$$

Four strategies listed below can be used to achieve the phase-matching condition to be fulfilled for FWM.

1. A low-intensity pump laser can be used for the FWM process; it leads to a reduction in frequency shift, meaning $2\gamma P$ is small, and if the $\Delta\beta$ is small enough, then phase

mismatch can be approximated to $\Delta\beta + 2\gamma P \approx 0$. Most of the time, the contribution from the Δk_W is quite small, and reducing the pump power also reduces the contribution from Δk_M and Δk_{NL}

2. Waveguide properties are adjusted for the wavelength of the pump laser where it experiences nearly zero dispersion; in other words, the group of velocity dispersion (GVD) becomes close to zero. It means linear phase mismatch term $\Delta\beta$ between the interaction waves is close to zero and can be compensated with nonlinear term $2\gamma P$. In this case, the phase matching condition $\Delta\beta + 2\gamma P = 0$ can be achieved by tuning the power of the pump laser, i.e., $\Delta k_W - (\Delta k_M + \Delta k_{NL}) = 0$

3. Similar to the nearly zero dispersion phase matching technique, waveguide properties can provide being in anomalous dispersion regime, meaning GVD is negative or dispersion is positive. In other words, linear phase mismatch ($\Delta\beta$) becomes negative. Thus, the nonlinear phase term ($2\gamma P$) can compensate for this negative mismatch by adjusting the pump power, i.e., $\Delta k_M - (\Delta k_W + \Delta k_{NL}) = 0$

4. Phase matching can be achieved by modal birefringence, in which the effective refractive index changes for different waveguide modes. Thus, control over the polarization states can be used for FWM.

In this thesis, the third technique (nearly zero dispersion) is used, which is a powerful and easy-to-achieve method. Advantageously, the slow dispersion change at near-zero dispersion wavelength provides phase matching for broadband pump wavelengths. As seen, the linear phase mismatch is small in this technique, so it requires a low-power pump laser, which is desired in most cases. Additionally, it can be said that it is more stable compared to the anomalous dispersion technique, meaning it can overcome fluctuations in the pump laser or small perturbations.

On the other hand, the anomalous dispersion technique can be more effective depending on its applications and can provide spectral broadening through self-phase modulation (SPM). Simply put, SPM is a phenomenon where the intense light pulse experiences varying refractive indexes during propagation, resulting in a time-dependent phase shift given as

$$\phi_{NL}(t) = \gamma P L_{eff} \tag{2.45}$$

where L_{eff} is the effective length of the waveguide. Regarding initial pulse shape is Gaussian, and it is described by a function $U(z,t)$ that undergoes spectral change given by

$$\delta\omega(t) = -\frac{\partial \phi_{NL}}{\partial t} = -\gamma P_0 L_{eff} \frac{\partial}{\partial t} |U(0,t)|^2 \tag{2.46}$$

2.1.2.2. Lugiato-Lefever Equation

Different parts of the pulse acquire different phase shifts, leading to frequency chirp, which is the reason for spectral broadening. This process is essential to create supercontinuum generation (SCG). To uncover how ultra-sharp pulse propagation occurs in nonlinear material, one must need a more complete model, which is described by a generalized nonlinear Schrödinger equation (GNSE)[6]:

$$\frac{\partial E}{\partial z} = -\frac{\alpha}{2}E + \sum_{k\geq 2} \frac{i^{k+1}}{k!}\beta_k \frac{\partial^k E}{\partial t^k} + i\gamma\left(1 + i\tau_s \frac{\partial}{\partial t}\right)\left(E(z,t)\int_{-\infty}^{+\infty} R(t')|E(z,t-t')|^2 dt'\right) \tag{2.47}$$

One mathematical model called the Lugiato-Lefever equation model, derived from GNSE, is used to describe and simulate Kerr-mediated nonlinear optical phenomena. This model enables the simulation of parametric frequency comb generation in the ring resonator based on the Lugiato-Lefever equation given by[7]

$$\frac{\partial E(z,\tau)}{\partial z} = -\frac{\alpha}{2}E + i\sum_{k>1} \frac{\beta_k}{k!}\left(i\frac{\partial}{\partial \tau}\right)^k E + i\gamma|E|^2 E \tag{2.48}$$

where $E(z,\tau)$ is a complex electric field propagating in the z-direction, τ is duration time, α is loss per unit length, γ is a nonlinear coefficient, n_2 Kerr index, and β_k is kth order of the Taylor expansion of propagation constant. This model describes the dispersion effect in the context of the evolution of complex field amplitude for a driven, damped Kerr-nonlinear ring resonator. For more information, refer to[7].

2.1.2.3. Kerr Effect

Considering the phase matching techniques, they rely on the nonlinear optical phenomenon known as the Kerr effect. This effect is crucial for the FWM process and indicates how the material's refractive index changes due to propagating light intensity. Intensity dependent refractive index is expressed as

$$n(\omega, I) = n_0(\omega) + n_2 I \tag{2.49}$$

where n_0 is the linear refractive index, I is the light intensity, and n_2 is the Kerr index, also known as the nonlinear index coefficient, and it is given as

$$n_2 = \frac{3}{4n_0^2\epsilon_0 c} \cdot \chi^{(3)} \tag{2.50}$$

Therefore, there is a linear relationship between n_2 and the third-order susceptibility $\chi^{(3)}$. The nonlinear parameter γ is given by the expression $\gamma = n_2\omega/cA_{eff}$. This coefficient takes place in the relationship between wave overlaps and phase-matching criteria. Therefore, having knowledge of n_2 allows us to determine the strength of the interactions. Furthermore, by tailoring waveguide geometry and material, it is possible to achieve a dispersion profile for an efficient FWM process.

2.1.3. Quantum Mechanical Description of Susceptibility

Expressions for nonlinear optical susceptibilities can be derived from the quantum mechanical framework, which covers the motivation to find susceptibilities' dependency on material properties such as atomic energy levels and dipole transition moments. The derived expressions also show the importance of internal symmetry of susceptibilities. Additionally, nonlinear optical susceptibilities can be numerically predicted to reveal the functionalities of materials. This section discusses the fundamental approach to finding nonlinear optical susceptibility. The main approach is to solve the time-dependent Schrödinger equation, which is

$$i\hbar\frac{\partial\psi}{\partial t} = \hat{H}\psi \tag{2.51}$$

and as a starting point, the Hamiltonian of the system is described by:

$$\hat{H} = \hat{H}_0 + \hat{V}(t) \tag{2.52}$$

where $\hat{H}_0$ is the Hamiltonian of the free atom and $\hat{V}(t)$ is the interaction Hamiltonian that represents the interaction between the atom and the applied electric field. The interaction Hamiltonian is given by

$$\hat{V}(t) = -\hat{\mu} \cdot \mathbf{E}(t) \tag{2.53}$$

$\hat{\mu}$ stands for electric dipole moment operator that is defined as $\hat{\mu} = -\hat{\mathbf{r}}$, where e is the charge of electron. Generally, given the Hamiltonian of the system in the equation (2.52), it cannot be solved exactly. To solve the Schrödinger equation, one may use perturbation theory. In this approach, a perturbation parameter is added to the interaction Hamiltonian, such as

$$\hat{H} = \hat{H}_0 + \lambda \hat{V}(t) \tag{2.54}$$

where λ is the perturbation parameter that ranges from zero to unity and indicates the strength of the interaction. Thus, λ can be written in power series, and the solution also takes the form of

$$\psi(\mathbf{r}, t) = \psi^{(0)}(\mathbf{r}, t) + \lambda \psi^{(1)}(\mathbf{r}, t) + \lambda^2 \psi^{(2)}(\mathbf{r}, t) + \cdots \tag{2.55}$$

$$i\hbar \frac{\partial \psi^{(0)}}{\partial t} = \hat{H}_0 \psi^{(0)} \tag{2.56}$$

$$i\hbar \frac{\partial \psi^{(N)}}{\partial t} = \hat{H}_0 \psi^{(N)} + \hat{V} \psi^{(N-1)}, \quad N = 1, 2, 3, \ldots \tag{2.57}$$

Equation (2.56) depicts the system's equation in the absence of an applied field and the solution is given by

$$\psi^{(0)}(\mathbf{r}, t) = u_g(\mathbf{r}) e^{-iE_g t/\hbar} \tag{2.58}$$

assuming system in the ground state and E_g represent the ground state energy, whereas a set of equations (2.57) reflects the system's equation under the condition of an applied field, and it can be solved using eigenfunctions of a free atom as a basis set

$$\psi^{(N)}(\mathbf{r}, t) = \sum_l a_l^{(N)}(t) u_l(\mathbf{r}) e^{-i\omega_l t} \tag{2.59}$$

where $a_l^{(N)}$ is the probability amplitude of N-th order and the ψ^N is the $N-th$-order contribution of wavefunction. The system of equation becomes if the equation (2.59) is substituted in equation (2.57)

$$i\hbar \sum_l \dot{a}_l^{(N)} u_l(\mathbf{r}) e^{-i\omega_l t} = \sum_l a_l^{(N-1)} \hat{V} u_l(\mathbf{r}) e^{-i\omega_l t} \tag{2.60}$$

Multiplying the equation (2.60) by u_m^* from left and side, taking integral and considering the orthonormality condition, the time derivative of the probability amplitude becomes

$$\dot{a}_m^{(N)}(t) = (i\hbar)^{-1} \sum_l a_l^{(N-1)}(t) V_{ml}(t) e^{i\omega_{ml}t} \tag{2.61}$$

where $\omega_{ml} = \omega_m - \omega_l$ representing frequency difference and V_{ml} is the matrix element of hamiltonian that is given as

$$V_{ml} \equiv \langle m|\hat{V}|l\rangle = \int u_m^* \hat{V} u_l \, d^3r \tag{2.62}$$

Thus N-th order probability amplitude can be found by

$$a_m^{(N)}(t) = (i\hbar)^{-1} \sum_l \int_{-\infty}^{t} dt' \, V_{ml}(t') a_l^{(N-1)}(t') e^{i\omega_{ml}t'} \tag{2.63}$$

Equation (2.63) indicates that if the N-1-th order of probability amplitude is known, then N-th order amplitude can be found by taking the time integral of N-1-th amplitude. Therefore, the procedure follows to initiate the system in the ground state, and then first, second, and higher-order amplitudes can be determined iteratively. To find $a_m^{(1)}$, a series of modifications are implemented on equation (2.63) as listed below.

1. Assuming system in ground state, $a_l^{(N-1)} = a_l^0$ is replaced by Kroneker-Delta function δ_{lg}.
2. $V_{ml}(t')$ is replaced by $-\sum_p \boldsymbol{\mu}_{ml} \cdot \boldsymbol{E}(\omega_p) \exp(-i\omega_p t')$
3. Electric-dipole transition moment $\boldsymbol{\mu}_{ml}$ is defined by $\mu_{ml} = \int u_m^* \hat{\mu} u_l \, d^3r$

By evaluating the integral on the modified equation yields $a_m^{(1)}$, and it can be used to calculate $a_n^{(2)}$. A similar fashion holds for $a_v^{(3)}$ and it is determined as

$$\begin{aligned} a_\nu^{(3)}(t) =& \frac{1}{\hbar^3} \sum_{pqr} \sum_{mn} \frac{[\mu_{vn} \cdot E(\omega_r)][\mu_{nm} \cdot E(\omega_q)][\mu_{mg} \cdot E(\omega_p)]}{(\omega_{vg} - \omega_p - \omega_q - \omega_r)(\omega_{ng} - \omega_p - \omega_q)(\omega_{mg} - \omega_p)} \\ & \times e^{i(\omega_{vg} - \omega_p - \omega_q - \omega_r)t} \end{aligned} \tag{2.64}$$

Determined $a_m^{(1)}$, $a_n^{(2)}$, and $a_v^{(3)}$ are substituted into equation (2.59) to find $\psi^{(1)}$, $\psi^{(2)}$, $\psi^{(3)}$ which are used to calculate nonlinear optical susceptibilities.

Considering the polarization equation (2.1), once the polarization is calculated, optical susceptibilities can be determined. At this point, the relationship between polarization and electric dipole moment is used, as defined by

$$\mathbf{P} = N\langle \mathbf{p} \rangle \tag{2.65}$$

where $\mathbf{P}$ is polarization, $\mathbf{p}$ is electric-dipole moment, and N is number density of atoms. In addition, the expectation value of the $\mathbf{p}$ is defined by

$$\langle \mathbf{p} \rangle = \langle \psi | \hat{\mu} | \psi \rangle \tag{2.66}$$

For the simplest case, i.e., $\chi^{(1)}$, the relation becomes $\mathbf{P^{(1)}} = N\langle \mathbf{p^{(1)}} \rangle$ and the expectation value of first-order electric dipole moment is given by

$$\langle \mathbf{p}^{(1)} \rangle = \langle \psi^{(0)} | \hat{\boldsymbol{\mu}} | \psi^{(1)} \rangle + \langle \psi^{(1)} | \hat{\boldsymbol{\mu}} | \psi^{(0)} \rangle \tag{2.67}$$

Substituting the $\psi^{(0)}$ and $\psi^{(1)}$ into the equation (2.67) and using the relation between polarization and $\chi^{(1)}$ that is given by

$$P_i^{(1)}(\omega_p) = \epsilon_0 \sum_j \chi_{ij}^{(1)} E_j(\omega_p) \tag{2.68}$$

The first-order optical nonlinear equation is found as

$$\chi_{ij}^{(1)}(\omega_p) = \frac{N}{\epsilon_0 \hbar} \sum_m \left(\frac{\mu_{gm}^i \mu_{mg}^j}{\omega_{mg} - \omega_p} + \frac{\mu_{gm}^j \mu_{mg}^i}{\omega_{mg}^* + \omega_p} \right) \tag{2.69}$$

The methodology for determining the $\chi^{(2)}$ and $\chi^{(3)}$ is similar to that used for first-order susceptibilities. To derive the $\chi^{(3)}$, expectation value of third-order electric-dipoles moment is written by

$$\langle \tilde{\mathbf{p}}^{(3)} \rangle = \langle \psi^{(0)} | \hat{\mu} | \psi^{(3)} \rangle + \langle \psi^{(1)} | \hat{\mu} | \psi^{(2)} \rangle + \langle \psi^{(2)} | \hat{\mu} | \psi^{(1)} \rangle + \langle \psi^{(3)} | \hat{\mu} | \psi^{(0)} \rangle \tag{2.70}$$

and third-order polarization is defined as

$$P_k(\omega_p + \omega_q + \omega_r) = \sum_{hij} \sum_{pqr} \chi_{kijh}^{(3)}(\omega_r, \omega_q, \omega_p) E_j(\omega_r) E_i(\omega_q) E_h(\omega_p) \tag{2.71}$$

Using the same analogy, $\chi^{(3)}$ is found as

$$\chi^{(3)}_{kijh}(\omega_\sigma, \omega_r, \omega_q, \omega_p) \equiv \frac{N}{\epsilon_0 \hbar^3} P_F \sum_{mnv} \frac{\mu^k_{gv}\mu^j_{vn}\mu^i_{nm}\mu^h_{mg}}{(\omega_{vg}-\omega_\sigma)(\omega_{ng}-\omega_q-\omega_p)(\omega_{mg}-\omega_p)} \tag{2.72}$$

where $\omega_\sigma = \omega_p + \omega_q + \omega_r$ and P_F is the full permutation operator that is described by

$$\begin{aligned}(-\omega_\sigma, \omega_q, \omega_p) \rightarrow &(-\omega_\sigma, \omega_p, \omega_q), (\omega_q, -\omega_\sigma, \omega_p), (\omega_q, \omega_p, -\omega_\sigma), \\ &(\omega_p, -\omega_\sigma, \omega_q), (\omega_p, \omega_q, -\omega_\sigma).\end{aligned}$$

The use of the full permutation operator guarantees the incorporation of all possible permutations of the frequency components since the nonlinear susceptibilities exhibit exchange symmetry on frequency components. In other words, it ensures all possible interactions between the input frequencies and output frequencies.

CHAPTER 3

OPTICAL WAVEGUIDE

3.1. Waveguiding

A waveguide aims for light confinement, enabling long propagation distances with minimum losses. Total internal reflection (TIR) occurs when light propagates through a substance and encounters a material with a lower refractive index at a greater than critical angle, resulting in waveguiding. Hence, refractive index contrast is essential for waveguiding. One of the most popular waveguides is optical fiber, illustrated in Figure (3.1.a), which allows long-distance communication via light. Standard optical fibers consist of a silica core surrounded by slightly lower-index silica cladding, achieved by doping the materials, and $10\mu m$ cored fiber is typically considered as single-mode fiber for telecommunication bandwidth.

A planar waveguide is another fundamental form of waveguide, which, as illustrated in Figure (3.1.b), consists of one planar core sandwiched by two planar cladding layers. In comparison to optical fiber, a planar structure is more feasible to fabricate for an integrated photonic platform, whereas fiber's cylindrical shape is favorable for mass production. Only these two types of geometrical waveguides can be analytically solved and designed. More complex geometrical designs need to be handled numerically. Although field confinement occurs only in the vertical direction in a planar waveguide, adding lateral confinement is possible with a strip waveguide with a core trimmed in horizontal and vertical dimensions, as shown in Figure (3.1.c). Strip waveguides can be produced with modern etching techniques, even bending them to maintain a ring shape integrated with a photonic structure such as a micro ring resonator. Figure (3.1.d) shows another waveguide form, namely rib waveguide, which has an additional narrower strip layer (rib) on top using the same or similar material. It requires at least two etching processes, which makes it complicated to fabricate compared to a strip waveguide. Although rib waveguides show more control on mode confinement for broad bandwidth, a larger effective area, and less loss, strip waveguides provide strong confinement and flexibility on bending. In this thesis, strip waveguide design is studied to achieve high confinement

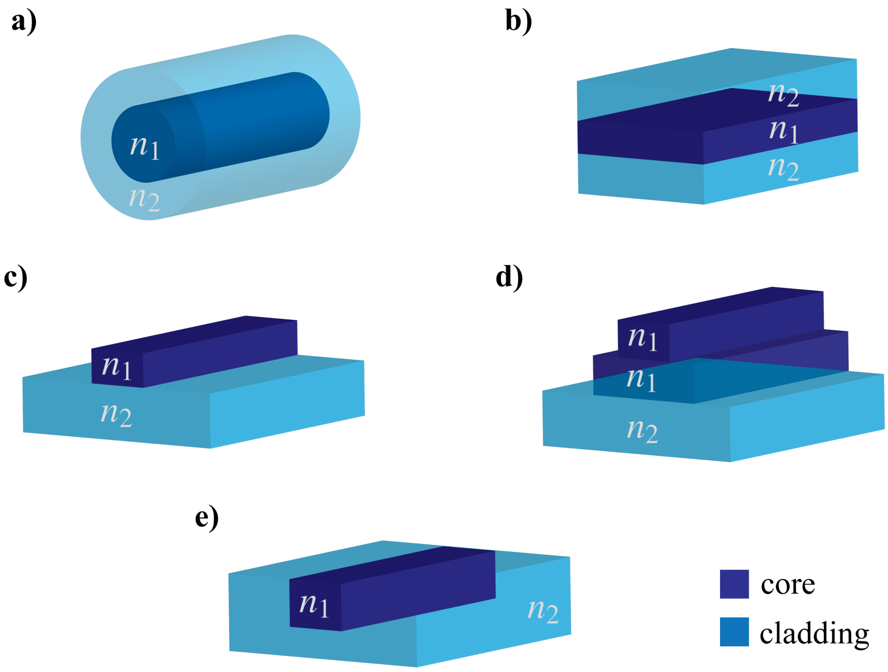

Figure 3.1. Representation of waveguide structures including: a) optical fiber, b) planar waveguide, c) strip waveguide, d) rib waveguide, and e) diffused waveguide.

and longer effective length with a ring resonator. Another waveguide type is a diffused waveguide, as shown in Figure (3.1.e). In this design, a high index region, the core, is created on the substrate due to the diffusion of dopants. One common example is the $LiNbO_3$ waveguide, where the core is made by the process of Ti diffusion. The diffusion process can be achieved through thermal diffusion, ion exchange, etc. This design brings the advantages of smoothly varying refractive index from core to cladding to reduce scattering losses. However, this smooth varying index does not allow for the achievement of high contrast in refractive index between core and cladding, resulting in a decrease in mode confinement. Another challenge is that this design requires a unique fabrication technique.

3.2. Material Based Nonlinear Optics

The polarization of a material plays a crucial role in producing third-order nonlinear interaction, as stated in section (2.1). Within this framework, crystalline silicon stands out as a favored platform due to its cubic lattice structure; third-order nonlinear effects can be clearly observed. The fact that physical phenomena such as the Kerr effect and Raman gain can be achieved in silicon-on-insulator (SOI) compact waveguides, even in the low power regime, has made silicon a material that is studied in areas such as telecommunications, stimulated Raman scattering, self and cross-phase modulation, and especially four-wave mixing. Following developments in integrated photonic circuits, research on silicon-based quantum light sources is a widely studied area in the literature. Lin and Agrawal demonstrated, for the first time, that photon pairs can theoretically be produced via SFWM in silicon-based waveguides[8]. This study shows that the production of highly correlated photon pairs is possible in the silicon waveguide due to the lack of spontaneous Raman scattering. Also, the spectral brightness of the photon pairs produced was found to be at a level comparable to other photon pair sources. In addition, the pump frequency is about 15.6 THz away from the silicon Raman spectrum. Therefore, if the pump frequency is set appropriately, generated photon pairs can be distinguished from scattered photons. Development in Si technologies has led to the experimental demonstration of correlated photon pair generation in Si waveguides[9]. Furthermore, the first time-bin entangled photon pair generation was demonstrated using a one-centimeter-long Si waveguide and CW telecom laser, reaching two-photon visibility to 0.73[10], which was then updated to 0.95 with the following research[11]. Besides, it has also been shown that polarization-entangled photon production is possible using Si waveguides[12,13]. Even though high confinement is necessary for nonlinear interaction, increasing interaction length is crucial for FWM process and can be achieved using a Si ring resonator, as shown in[14,15]. Besides, energy-time-entangled photon pair generation[16] and supercontinuum generation[17] were demonstrated using a Si ring resonator and Si waveguide, respectively.

Although the success of the Si platform for nonlinear optics shows phenomena such as FWM, photon pair, and entangled photon generation, it exhibits two-photon absorption, as reported in[18,19] for telecom wavelengths, due to photons exceeding its half-band energy. This makes it necessary to study other platforms, namely chalcogenides[20,21,22,23,24], III-IV materials[25,26,27,28], and CMOS-compatible, for nonlinear optical processes in the literature.

This thesis primarily focuses on using CMOS-compatible materials, such as silicon nitride. These compatible materials have garnered interest in nonlinear optics due to the low cost and mass production of CMOS technologies. Since silicon nitride is widely used in integrated photonic circuits, has a large transparency window, and has a high Kerr coefficient, it is an ideal choice for enhancing nonlinear processes.

Other nonlinear materials compatible with CMOS technologies, such as stoichiometric silicon nitride, are also used. Stoichiometric silicon nitride provides lower propagation loss[29], a higher quality factor[30], and reduced two-photon absorption. However, complex fabrication is required due to the formation of high stress while depositing a thick layer, which causes cracking. Using this material, Kerr frequency comb generation in the resonator has been shown[31,32,33]. The cracking issue of this material can be overcome by changing the ratio of silicon and nitride, which alters the mechanical properties of the material. This kind of material is known as silicon-rich nitride. Although it provides higher refractive index contrast and Kerr index, reducing band gap energy causes two-photon absorption. Additionally, silica-based glass, also known as Hydex, is used for nonlinear optical applications such as FWM in ring resonators[34], supercontinuum[35], and frequency comb generation[36,37].

3.3. Eigen-Mode Solution

The Eigenmode of the waveguide refers to the electromagnetic field profile that propagates through the waveguide without being affected by any disturbances that alter its shape. These modes are found from solution Maxwell's equations using boundary conditions determined by waveguide structure. Offering uniformity along one axis is important in the waveguide geometry. Thus, the spatial dependence of the dielectric constant decreases since it only exhibits lateral dependence. Conventionally, this uniformity is represented in z-coordinate; therefore, the dielectric constant is written as $\varepsilon(\mathbf{r}_\perp)$, where $(\mathbf{r}_\perp)$ indicates plane constituted in x-y coordinates which is normal to z-coordinate.

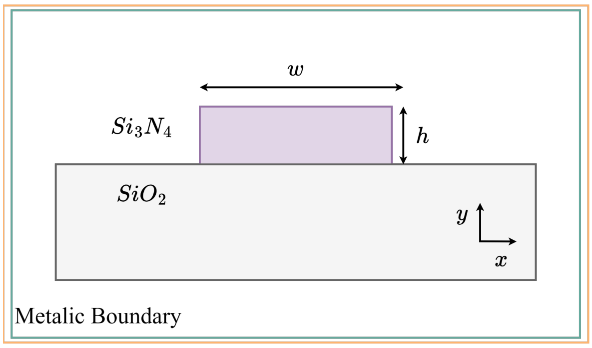

Figure 3.2. Cross-section of strip waveguide and its dimensions

Figure (3.2) shows the cross-section of the strip waveguide that is used in this thesis. In this geometry, the waveguide is invariant along the z direction, which brings some important consequences. The first one removes one dimension of the dielectric constant, hence eliminating the z-derivatives arising from Maxwell's equations. This simplification speeds up the computation process to find the mode profile of the waveguide. The following advantage is it allows us to write the electric field of the propagation wave as

$$\mathbf{E}(\mathbf{r}) = \mathbf{e}(\mathbf{r}_{\perp})e^{i\beta z} \tag{3.1}$$

where $\mathbf{e}(\mathbf{r}_1)$ is the transverse spatial distribution of the field, and β is the propagation constant. The waveguide material in this thesis, silicon nitride, is dielectric, non-magnetic, and lacks free charge and current. Thus, the optical modes of the waveguide are the eigenstates, and propagation constants are the square root of eigenvalues of the modal vector wave equation that is given by[38]

$$\nabla_{\perp}^{2}\mathbf{e}_{\perp} + \nabla_{\perp}(\mathbf{e}_{\perp} \cdot \nabla \ln \varepsilon(\mathbf{r}_{\perp})) + \varepsilon(\mathbf{r}_{\perp})k_0^2\mathbf{e}_{\perp} = \beta^2\mathbf{e}_{\perp} \tag{3.2}$$

where k_0 is the wavenumber and β is the propagation constant.

The finite difference element method based on Lumerical MODE solution is used to find the waveguide's mode profile and dispersion characteristics based on the procedure[39]. This approach includes the process of discretizing the cross-section of the waveguide by meshing, which provides a way to handle complex structures. Nevertheless, By increasing the discretization, one may get accurate computation. Once the meshing is constructed, Maxwell's equations are formulated according to this discretization. It provides for writing partial differential equations in a system of linear algebraic equations, which can be represented as a matrix eigenvalue problem indicated in equation (3.2). Therefore, the sparse matrix technique can be used to solve eigenvalue problems efficiently.

3.4. Disperison Engineering

Light propagating in a material, in this case, a waveguide structure, encounters varying refractive indices at various wavelengths. This phenomenon is called dispersion. In other words, the propagation constant of each mode of the waveguide is dependent on the wavelength of the light. Dispersion explains phenomena such as two pulses with different wavelengths exhibiting varying group and phase velocities inside the same waveguide. It is also responsible for pulse broadening, which is critical for supercontinuum generation. The waveguide dispersion profile plays a critical role in determining the phase-matching requirement for the FWM process, as discussed in section (2.1.2.1). The modification of the phase velocities of the interacting wave gives rise to wavelength conversion and photon pair generation. The waveguide dispersion profile depends on its dimension; therefore, tailoring the waveguide geometry can enhance the FWM efficiency, which is significant for optical communication and photonic applications.

Introducing parameters is the first step to determining the characteristics of the waveguide mode. Therefore, the first parameter is the effective refractive index, which shows how light propagates inside the waveguide and includes information about the material and waveguide structure. The effective refractive index is defined as

$$n_{\text{eff}} = \frac{\beta}{k_0} \tag{3.3}$$

where $k_0 = 2\pi/\lambda_0$ and β is the propagation constant.The effective refractive index of a waveguide varies with the wavelength of the light, and various modes of waveguide have different effective refractive indexes. The effective refractive index is used when designing the waveguide geometry and selecting the core and cladding materials. As stated in the equation (3.4), the effective refractive index must be lower than the core's refractive index and greater than the cladding's refractive index for waveguiding to occur.

$$n_{\text{cladding}} \leq n_{\text{eff}} \leq n_{\text{core}} \tag{3.4}$$

Figure (3.3) displays the refractive indices of Si_3N_4 and SiO_2 in comparison to the waveguide's effective refractive index as a function of wavelength. The waveguide's height is 460 nm, and its width is 570 nm, and this geometry satisfies the waveguiding condition in equation (3.4) for a 780 nm pump field. The waveguiding condition indicates how much the electric field of the corresponding mode is confined within the waveguide's core. If the effective refractive index is close to the effective index of the core, the electric field is tightly confined inside the core. In contrast, if the effective index is close to the cladding's refractive index, the electric field confinement tends to leak into the cladding. In other words, the spatial distribution of the electric field of the corresponding mode lies inside the core for a higher effective refractive index, whereas a lower effective refractive index causes a more extended evanescent field inside the cladding. This wavelength dependency allows for the engineering of the waveguide geometry, such as increasing the evanescent wave for efficient coupling to other photonic devices like ring resonators or increasing field confinement inside the core to achieve higher nonlinear interaction for efficient conversion. In the case of the Silicon nitride waveguide, as the wavelength of the pump field decreases, there is a greater degree of confinement inside the core.

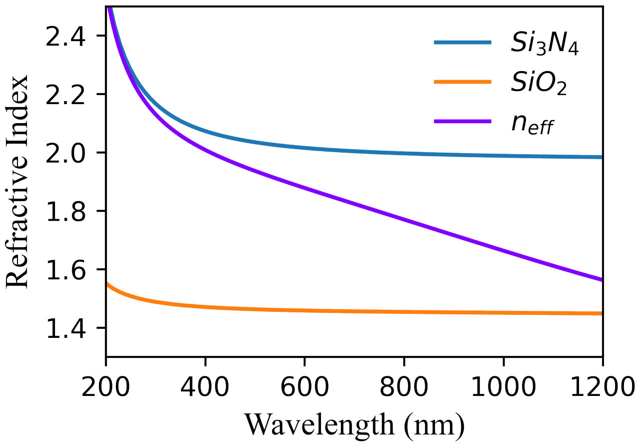

Figure 3.3. The refractive index of Si_3N_4, SiO_2, and the effective index as a function of wavelength for a waveguide with a height of 460 nm and a width of 570 nm.

Figure (3.4) shows the geometry dependence of the effective refractive index. By sweeping the waveguide's height and width by 50 nm steps, the effective refractive index is calculated for the 780 nm pump field. From this figure, it is clear that increasing the section area of the waveguide causes an increase in the effective refractive index. However, it only indicates that most of the electric field lies inside the core; it does not show how dense it is at the center of the core.

To gain more information on this wavelength dependency and phase shift inside the waveguide, the propagation constant is expanded in the Taylor series around the center frequency, i.e., $\beta_m = \left(\frac{d^m\beta}{d\omega^m}\right)_{\omega=\omega_0}$:

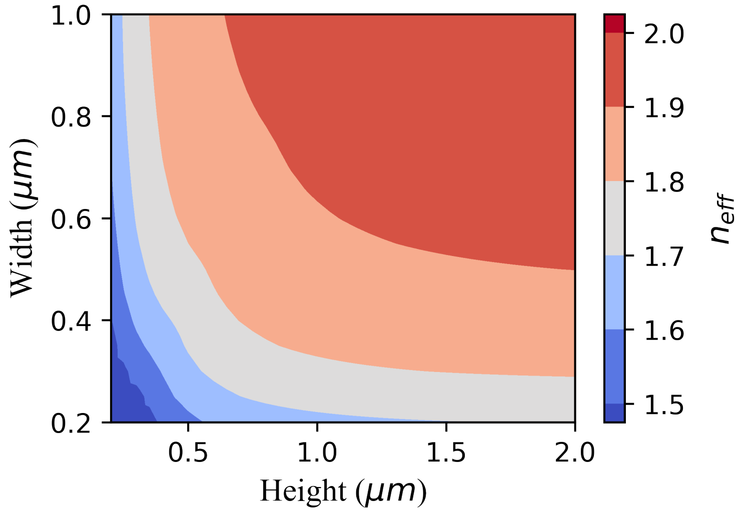

Figure 3.4. The effective index of a Si_3N_4 waveguide as a function of its height and width at a 780 nm pump wavelength

$$\beta(\omega) = n(\omega)\frac{\omega}{c} = \beta_0 + \beta_1(\omega - \omega_0) + \frac{1}{2}\beta_2(\omega - \omega_0)^2 + \frac{1}{6}\beta_3(\omega - \omega_0)^3 + \dots \tag{3.5}$$

where β_m is a different contribution to the propagation constant, increasing order of propagation constant represents different propagation effects. β_0 is related to the phase velocity of the propagation field by $v_p = \frac{\omega_0}{\beta_0}$ and the first order of the propagation constant β_1 is linked to group velocity and group index, such as:

$$\beta_1 = \frac{1}{v_g} = \frac{n_g}{c} = \frac{1}{c}\left(n + \omega\frac{dn}{d\omega}\right) \tag{3.6}$$

where v_g is group velocity and n_g is group index. Group velocity is defined as the velocity of the wave envelope through the material. Considering the FWM process, four different frequency components have different group velocities, which impact the phase-matching requirement, and the group index is the ratio of the speed of light in a vacuum to the group velocities of wavepackets ($n_g = \frac{c}{v_g}$). A higher group index (lower group velocity) increases the nonlinear interaction through the waveguide or ring resonator due to increasing interaction time, leading to an efficient FWM process. Moreover, the distance between the resonance peaks (Free Spectral Range, abbrev. FSR) of the ring resonator is also inversely proportional to the group index.

$$FSR \propto \frac{1}{n_g} \tag{3.7}$$

Increasing the group index causes a small FSR. Controlling the group index is crucial to designing the ring resonator with the desired FSR, where applications such as photon pair generation FSR want to be big enough to separate the photon pair by wavelengths with optical filters. Figure (3.5) shows group index and group velocity as a function of wavelength for 460 nm thick and 570 nm wide silicon nitride waveguide.

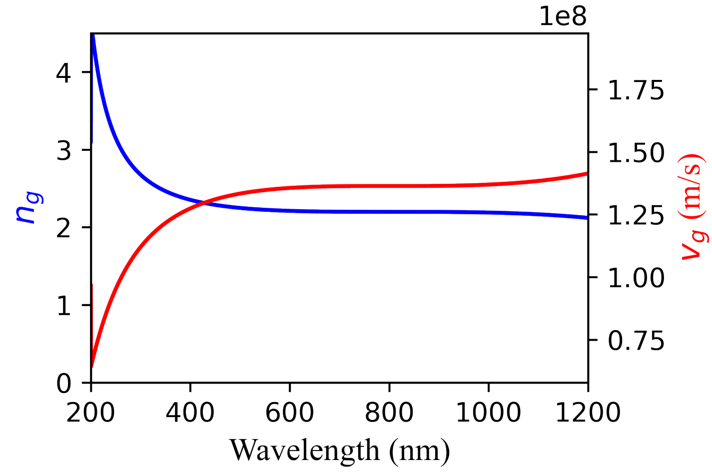

Figure 3.5. n_g and v_g of a Si_3N_4 waveguide with 460 nm height and 570 nm width as a function of wavelength.

The second-order propagation constant represents the group velocity dispersion (GVD), and it is related to β_1 as $\beta_2 = \frac{d\beta_1}{d\omega}$:

$$\beta_2 = \frac{1}{c}\left(2\frac{dn}{d\omega} + \omega\frac{d^2n}{d\omega^2}\right) \tag{3.8}$$

Using GVD, the dispersion parameter, D, can be written as:

$$D = \frac{d\beta_1}{d\lambda} = -\frac{2\pi c}{\lambda^2}\beta_2 = -\frac{\lambda}{c}\frac{d^2n}{d\lambda^2} \tag{3.9}$$

Figure (3.6) shows the calculation of dispersion and group velocity dispersion for a silicon nitride waveguide with a width of 570 nm and a height of 460 nm.

The sign and value of dispersion explain the temporal broadening of the different frequency components during the propagation inside the waveguide. The dispersion characteristic is distinguished by two different regimes known as normal and anomalous dispersion. Different scenarios for dispersion regimes are listed below:

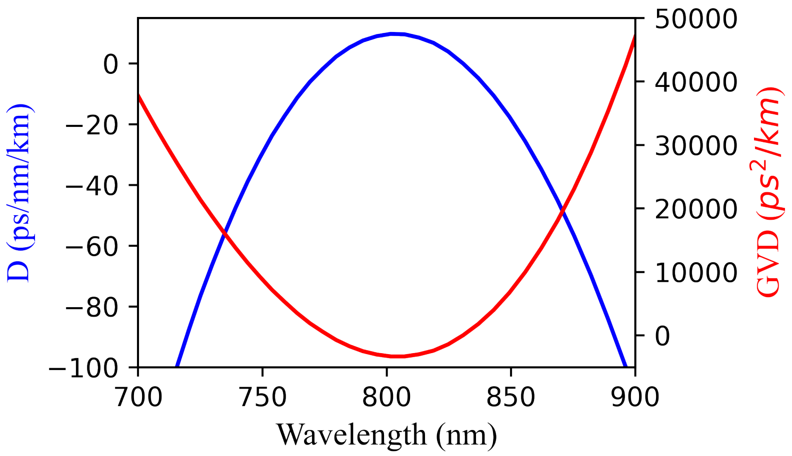

Figure 3.6. D and GVD of a Si_3N_4 waveguide with 460 nm height and 570 nm width as a function of wavelength

1. Most of the material shows normal dispersion that occurs D<0 (GVD>0). In this regime, longer-wavelength components propagate faster than shorter ones. Therefore, the leading edge (high wavelength) of the pulse arrives at the end of the wavelength. It can cause an up-chirped and stretched pulse.
2. In anomalous dispersion D>0 (GVD<0), this regime leads shorter wavelength components to propagate faster than longer ones and can cause a reversal of the color order during the propagation. The pulse can possess down-chirping and compression because the trailing edge (lower wavelength) passes the leading edge (higher wavelength). Additionally, the anomalous dispersion regime plays a crucial role in achieving phase matching for the FWM process that is mentioned in Section (2.1.2.1).

Dispersion characteristics can be engineered by changing the dimensions of the waveguide. In this thesis, one of the main goals is to achieve phase matching via the near-zero dispersion method; therefore, the waveguide is tailored where the pump laser is in the anomalous regime and quite close to the zero dispersion wavelength (ZDW). Besides, it is considered that the waveguide dimension leads to high modal confinement for efficient nonlinear interactions. To determine optimal waveguide geometry, the waveguide dimensions are varied in steps of 50 nm for both its height and width, and dispersion is calculated for 780 nm pump wavelength and multi-coefficient fitting to silicon nitride refractive index data which is shown in Figure (3.7) is used. Without proper fitting, it is observed that artifacts occur in calculations.

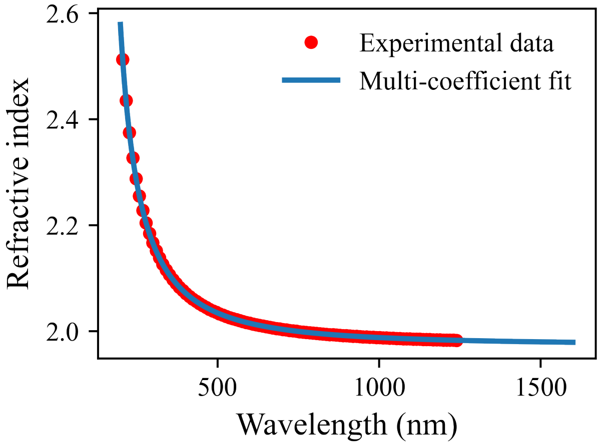

Figure 3.7. Multi-coefficient fitting to experimentally provided refractive index of Si_3N_4[1]

Figure (3.8) shows the results of the dispersion calculation in relation to the dimension of the waveguide. Sweeping a wide range of width and height gives insight into the appropriate geometry of the waveguide where the pump wavelength is close to ZDW. Based on the calculations, it is feasible to acquire proper geometry, where dimensions are within the range of $500 - 600$ nm for width and $350 - 500$ nm for height, and this range is boxed in the figure. For this reduced range of waveguide dimensions, a more precise computation is performed by varying the width and height in increments of 10 nm while also increasing the number of wavelength points.

Another important parameter for designing a waveguide is the effective mode area, which is given by

$$A_{\text{eff}} = \frac{\left(\int\int_{-\infty}^{+\infty} |E(x,y)|^2 \, dx \, dy\right)^2}{\int\int_{-\infty}^{+\infty} |E(x,y)|^4 \, dx \, dy} \tag{3.10}$$

The effective mode area quantifies the degree of spatial confinement of the supported modes, a crucial quantity to consider in nonlinear interactions. A smaller effective mode area results in a more confined pump laser, leading to higher power for the FWM process. It is assumed that the mode profile doesn't change during the propagation inside the waveguide. The effective mode area as a function of waveguide height and width at a pump wavelength of 780 nm is shown in Figure (3.9). As the figure shows, increasing

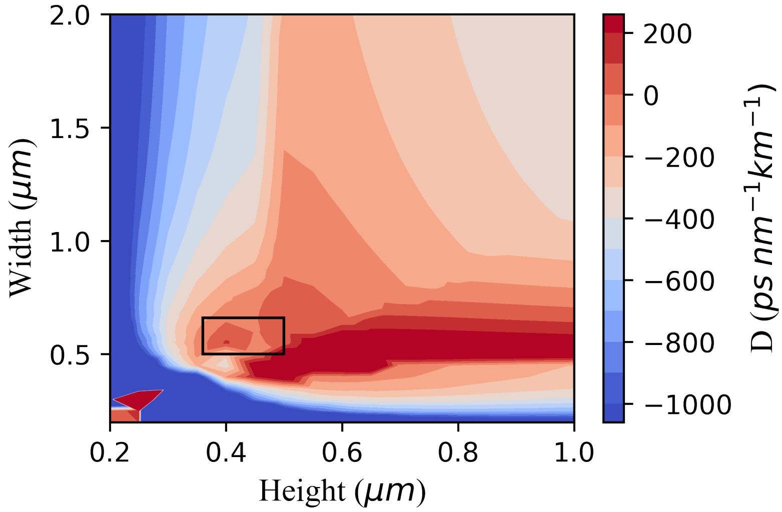

Figure 3.8. Dispersion of a Si_3N_4 waveguide as a function of its height and width at a 780 nm pump wavelength

the waveguide size leads to an increase in the effective mode area. Therefore, smaller dimensions are preferable to obtain high-intensity confinement.

The nonlinear parameter is inversely proportional to the effective mode area, which is indicated as

$$\gamma \approx \frac{n_2\omega}{cA_{eff}} \tag{3.11}$$

The calculation of the nonlinear parameter for the silicon nitride waveguide at pump 780 nm pump wavelength, where the dimensions vary, is shown in Figure (3.10). In this calculation, the Kerr index is taken from the literature, which is $n_2 = 2.4 \cdot 10^{-19} m^2 W^{-1}$.

Considering Figures (3.8) and (3.10), a comparison of dispersion and nonlinear parameter calculations for waveguides with changing dimensions shows that the ZDW region is not far away from a high nonlinear parameter region. Without sacrificing spatial confinement, near-zero dispersion phase matching is possible. This is an advantage of using a silicon nitride waveguide at the 780 nm pump wavelength.

Figure (3.11) demonstrates the wavelength dependence of nonlinear parameters. For a waveguide with 460 nm height and 570 nm width, increasing the pump wavelength decreases the nonlinear parameter, which indicates that using a high-frequency pump laser makes the nonlinear process more efficient.

A near-zero dispersion regime for the 780 nm pump wavelength is achieved for a

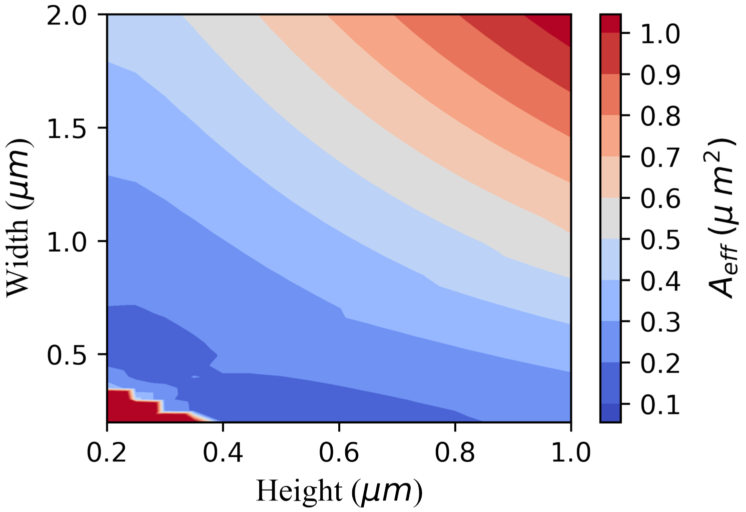

Figure 3.9. The effective area of a Si_3N_4 waveguide as a function of its height and width at a 780 nm pump wavelength

waveguide with 460 nm height and 570 nm width. The dispersion value for this waveguide is found to be D = 2.25 at a wavelength of 780 nm. The peak point of the dispersion curve occurs at a wavelength of 801 nm, which has a dispersion value of around 9.7. The dispersion curves are shown in Figure (3.12), where the height remains constant at 460 nm while the width varies.

To achieve broadband phase matching for FWM, the peak point of the dispersion curve is desired to occur at the pump wavelength. In Figure (3.13), the dispersion curves for the 780 nm wavelength are shown, where height is constant at 460 nm while width is varying. As seen in the figure, the peak point occurring at 780 nm is achieved for a waveguide with a height of 450 nm and a width of 470 nm. Although this waveguide structure provides high confinement of the field, the dispersion value is quite far away from the near-zero dispersion regime.

Furthermore, the parametric gain resulting from the coupled differential equations is given by

$$g_p = \sqrt{(\gamma P)^2 - \left(\frac{\kappa}{2}\right)^2} \tag{3.12}$$

Equation (3.12) demonstrates how the amplification strength is influenced by the effective phase mismatch κ. The graph in Figure (3.14) displays the calculated parametric gain for a waveguide with a height of 460 nm and a width of 570 nm, with varying pump

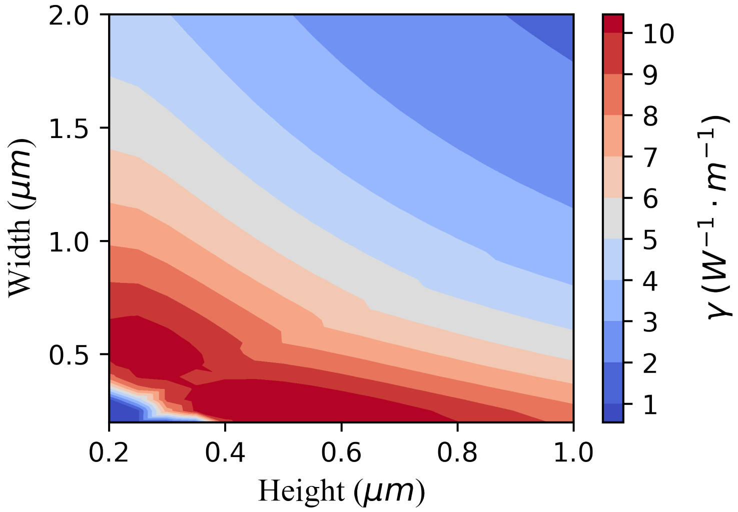

Figure 3.10. Nonlinear parameter of a Si_3N_4 waveguide as a function of its height and width at a 780 nm pump wavelength

power. The x-axis of the figure represents the wavelength difference between the signal and idler waves. It is evident that maximum gain occurs when the phase mismatch is zero for all pump powers. Furthermore, the shape of the gain can be adjusted for different waveguide dispersion values and the bandwidth of the gain changes with varying pump power.

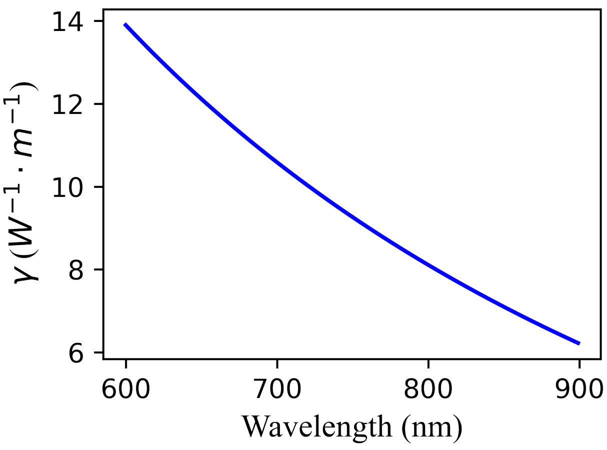

Figure 3.11. Nonlinear parameter of a Si_3N_4 waveguide with 460 nm height and 570 nm width as a function of wavelength

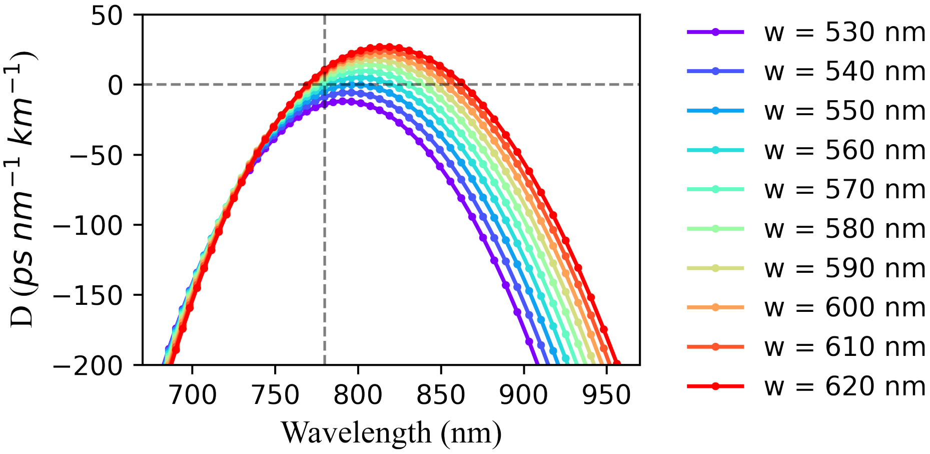

Figure 3.12. Dispersion curve of a Si_3N_4 waveguide with 460 nm height and varying widths as a function of wavelength

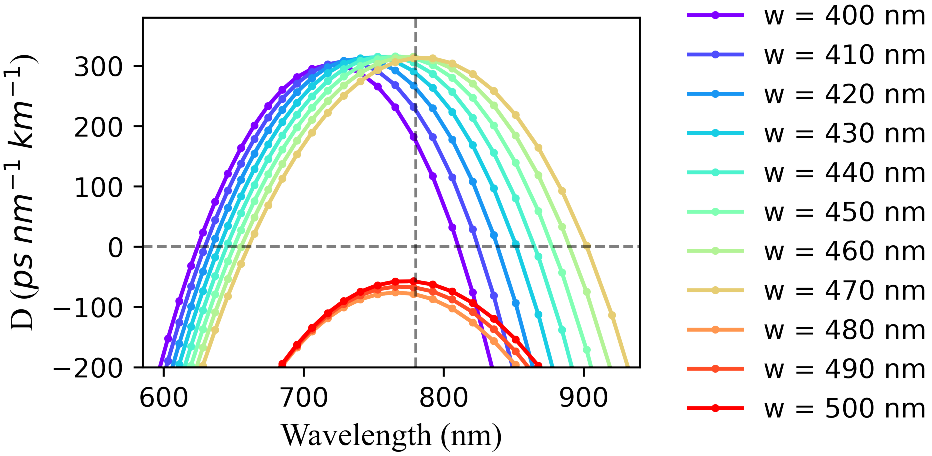

Figure 3.13. Dispersion curve of a Si_3N_4 waveguide with 450 nm height and varying widths as a function of wavelength

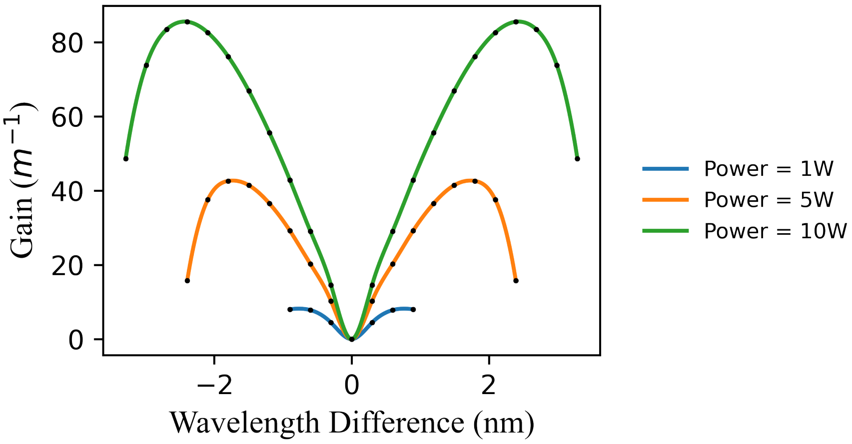

Figure 3.14. Parameter gain of a Si_3N_4 waveguide with 460 nm height and 570 nm width as a function of wavelength difference between signal and idler waves

3.4.1. Mode Profile

The mode profile of the waveguide refers to the spatial distribution of the electric and magnetic field of the corresponding mode on the cross-section of the waveguide. The mode of the waveguide is calculated by solving the Maxwell equation, and the shape of the mode does not change during propagation in the waveguide if the losses are negligible. By definition, the fundamental mode is the lowest order mode with no nodes, and conventionally, TE modes are chosen where the polarization of the field lies on the x-axis. Similarly, primarily polarized in the y-axis modes are called TM modes. Subscripts of modes such as TE_{00} (fundamental mode) indicate the number of nodes. The first subscript corresponds to the x-axis, and the second one corresponds to the y-axis. Figure (3.15) shows the first four modes of a waveguide with a height of 460 nm and a width of 570 nm. Figure (3.15a, b, c, and d) represent the modes arranged in ascending order. Figure (3.15 a) corresponds to the fundamental mode of the waveguide, TE_{00} mode. On the other hand, Figure (3.15b) relates to the TM_{00} mode. Effective refractive indices are indicated for each mode profile, which decreases as the mode order increases. The polarization fraction of modes for the x-axis is given by

$$\text{TE polarization fraction (Ex)} = \frac{\int |E_x|^2 \, dx \, dy}{\int (|E_x|^2 + |E_y|^2) \, dx \, dy} \tag{3.13}$$

For a waveguide with 460 nm height and 570 nm width, TE_{00} is found to be totally polarized on the x-axis, and TM_{00} mode's polarization is totally on the y-axis. In addition, the effective mode area is found to be $0.23 \mu m^2$.

The propagation loss can be calculated in mode solution using complex refractive index such as $n + i\kappa$, where κ refers to the imaginary part of the refractive index. Hence, the electric field for propagation wave can be written as

$$E(z) = e^{i2\pi(n+i\kappa)z/\lambda_0} \tag{3.14}$$

Considering propagation loss is given by

$$\text{loss} = -10\log_{10}\left(\frac{P(z)\big|_{z=1\,\mathrm{m}}}{P(z)\big|_{z=0\,\mathrm{m}}}\right) = -10\log_{10}\left(\frac{|E(1)|^2}{|E(0)|^2}\right) = -20\log_{10}\left(\frac{|E(1)|}{|E(0)|}\right) \tag{3.15}$$

substituting the equation (3.14) yields

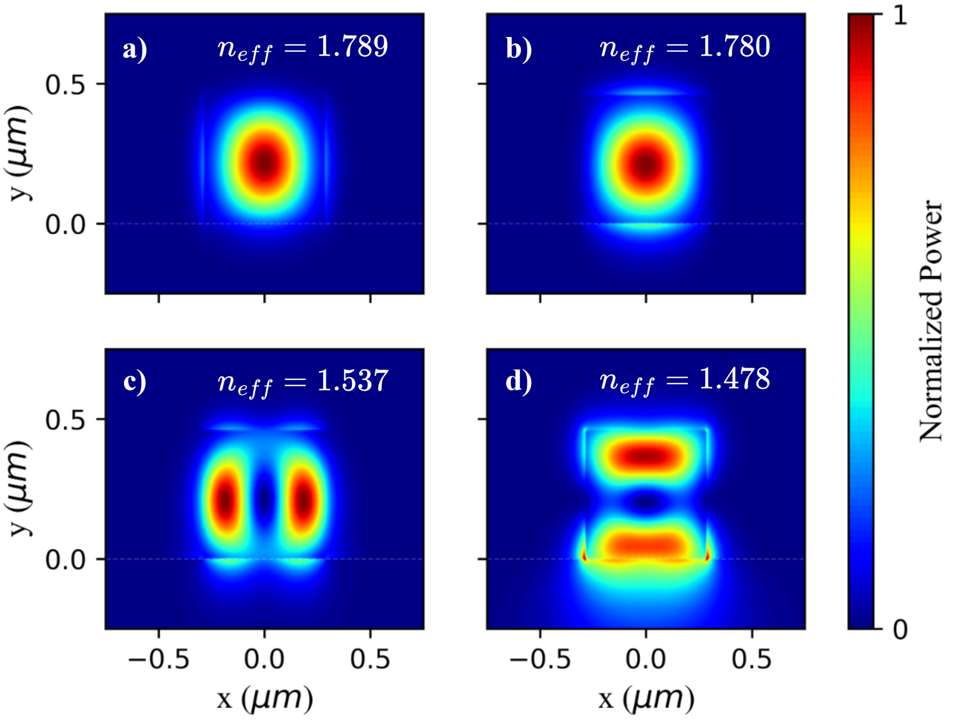

Figure 3.15. First four mode profiles of a waveguide with a 460 nm height and 570 nm width

$$\text{loss} = -20\log_{10}\left(e^{-2\pi\kappa/\lambda_0}\right) \tag{3.16}$$

The propagation loss for a waveguide with a height of 460 nm and width of 570nm is 0.0092 dB/cm.

CHAPTER 4

RING RESONATOR

A ring resonator is an integrated optical device that offers many advantages, such as wavelength filtering and multiplexing, modulation of optical signals, and photon pair generation. It is used in many different quantum applications, including quantum key distribution, quantum computing, and quantum metrology. In this thesis, add-drop microring resonator configuration is studied, as illustrated in the figure. The arrangement contains a microring resonator (closed-looped waveguide) positioned between two bus waveguides. Light coming from the input port, its evanescence wave can couple to a ring resonator, which allows the light that is resonant to the microring to circulate. This circulation arises when the light constructively interferes inside the ring resonator. With this, when the light is confined in a round-shaped dielectric material, it experiences total internal reflection after each round trip, resulting in the formation of whispery gallery modes. To achieve constructive interference, the length of the ring resonator must be multiple integers of the wavelength of the light that is given by

$$2\pi R = m\lambda \tag{4.1}$$

where R is the radius of the ring resonator, and m is the integer number. In the context of FWM, if the resonant condition is satisfied via constructive interference, light intensity is significantly increased, which enhances nonlinear interaction. This statement is closely related to the quality factor of the resonator, which quantifies the amount of stored energy. The chapter aims to investigate the ring resonator properties in a way to achieve efficient nonlinear interactions.

The spectral characteristics of the silicon nitride microring resonator are investigated using the finite difference time domain method based on Lumerical var-FDTD solution. In this method[40], instead of using a two-dimensional planar monitor to find the transmission of ports, a linear monitor placed inside the waveguide along with the polarization direction of the electric field is used to speed up the computational time. The figure shows the light source positioned at the input port. According to the waveguide's mode profile calculation, the 780 nm pump light that is placed to the input port and its polarization direction is adjusted to the x-axis because the waveguide's fundamental mode is polarized along the x-axis. Moreover, monitors are placed on outputs and inside the ring resonator to measure the transmission.

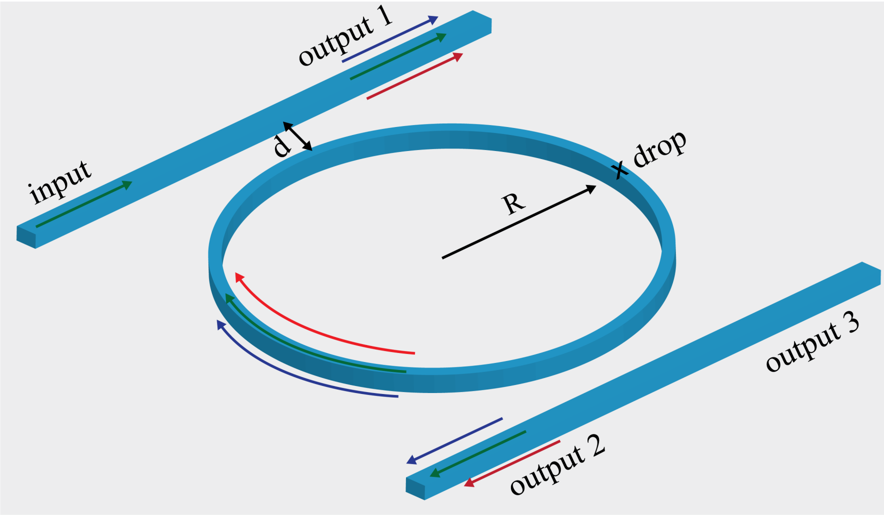

Figure 4.1. Representation of all pass ring resonator structure

A crucial design parameter known as the free spectral range (FSR) is considered to determine the radius of the ring resonator. The FSR is given by

$$\mathrm{FSR} = \frac{\lambda^2}{n_g L} \tag{4.2}$$

FSR represents the distance between the resonance wavelength peaks of the ring resonator, and it is inversely dependent on the ring's round trip length and the waveguide's group index. The group index is calculated from the effective index as

$$n_g = n_{\text{eff}} - \lambda_0 \frac{dn_{\text{eff}}}{d\lambda} \tag{4.3}$$

The waveguide, which has a height of 460 nm and a width of 570 nm, has a calculated group index of 2.19 at the pump wavelength of 780 nm. Also, the desired FSR is considered at least to be 5 nm, indicating that there should be a spectral separation of 10 nm between the signal and idler waves. This separation is quite enough to distinguish idler and signal waves with the optical instruments in the experimental study scenario. Based on these values, the radius of the ring resonator is determined to be approximately 10 μm.

The finesse (F) of a ring resonator is another parameter that measures the sharpness of the resonance peaks. It indicates the presence of a highly confined field inside the resonator and is defined as the ratio of the FSR to the resonance's linewidth.

$$F = \frac{\text{FSR}}{\text{FWHM}} \tag{4.4}$$

Finesse is also related to a quality factor commonly used to describe the resonator's performance and efficiency. It explains how much energy is stored during each round trip before being lost from the resonator due to internal losses and coupling to the bus waveguide. Thus, the quality factor of the all-pass ring resonator is considered to be greater than that of all drop ring resonators. In this thesis, all drop ring resonators are used to achieve feasible simulation time for computational power. Besides, the quality factor is found as the number of oscillations of the field inside the resonator before it is reduced to 1/e of the initial energy; similarly, finesse indicates the number of round trips before reaching 1/e to its initial energy. From this point of view, reducing round trip and coupling losses leads to achieving high-quality factor resonators. In addition, the quality factor is defined by

$$Q = \frac{\lambda_{\text{res}}}{\text{FWHM}} \tag{4.5}$$

Regarding the relationship between finesse and quality factor and taking FWHM as a common parameter, the quality factor can be expressed as

$$Q = \frac{n_g L}{\lambda} F \tag{4.6}$$

Using the analogy from the Fabry-Perot cavities, finesse can be expressed as

$$\text{F} = \frac{\pi \left| t_{11} \right|}{1 - \left| t_{11} \right|} \tag{4.7}$$

where τ_{11} is the transmission coefficient to output 1 port. The quality factor then becomes

$$Q = \frac{n_g L \pi}{\lambda} \frac{\left| \tau_{11} \right|}{1 - \left| \tau_{11} \right|^2} \tag{4.8}$$

It is assumed that there is no loss in this expression. For analytical investigation, the loss contribution from each part can be added to the quality factor. While this equation suggests that increasing the group index and round trip length of the resonator can lead to an increased quality factor, it should be noted that this modification can also cause an increase in losses. Furthermore, the equation indicates that reducing the wavelength causes a higher quality factor.

4.1. FDTD Solution

This section presents outcomes obtained from FDTD simulation of the silicon nitride ring resonator. One critical condition for constructing an FDTD simulation is choosing the right meshing step size and simulation times. This affects the accuracy and robustness of the results because FDTD methods handle discrete functions. Thus, to determine simulation time, a constraint on the time step δt is taken into account. If dδt is too big, it causes unnecessary simulation time. Conversely, if δt is too small, it results in imprecise outcomes. There is an inequality that connects the mesh step size and time step known as Courant stability criterion or Courant-Friedrichs-Lewy condition, and it is given by[38]

$$\delta t \leq \frac{1}{c_0}\left\{\left(\frac{1}{\delta x}\right)^2+\left(\frac{1}{\delta y}\right)^2+\left(\frac{1}{\delta z}\right)^2\right\}^{-1/2} \tag{4.9}$$

Therefore, the 3D meshing time step becomes

$$\delta t \leq \frac{\delta x}{c_0\sqrt{3}} \tag{4.10}$$

On the other hand, a reasonable step size of mesh in the form of wavelength is given by[38]

$$N_\lambda = \frac{\lambda_0}{\delta x} \geq 10n \tag{4.11}$$

where λ_0 is the vacuum wavelength, and n is the refractive index of the medium. Thus, the required mesh step is chosen, and In Lumerical FDTD solutions, while the mesh step size is adjusted, the time step is automatically chosen according to the given condition (4.10).

Figure (4.2) shows the transmission spectrum of the ring resonator on output 1 port where the gap distance between the bus waveguide and microring is 75 nm. In this and following simulations, the mesh step size is considered to give an accurate result. The radius of the ring is chosen to be 10 μm. In addition, the waveguide dimension is taken to be a height of 460 nm and a width of 570 nm.

To determine the optimal distance for effective coupling of the evanescent wave to the ring resonator, a simulation is conducted, where the transmission through the ring is simulated. The gap distance varies from 0 to 200 nm, while the radius is fixed. In this simulation, the wavelength range is taken to cover only signal, pump, and idler waves. The result is shown in Figure (4.3), which represents the power measurement of waves

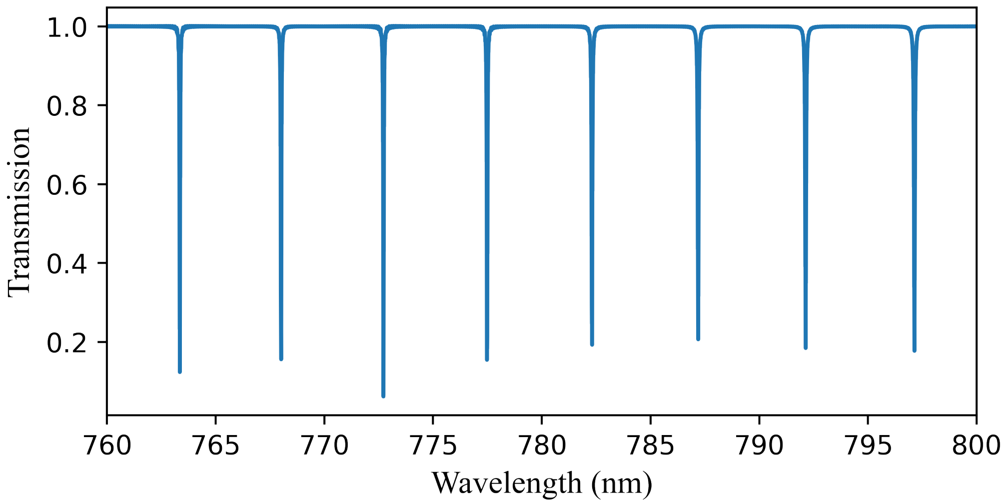

Figure 4.2. Transmission spectrum of a Si_3N_4 resonator with a 460 nm height and 570 nm width, and 10 μm radius from output 1 port as a function of wavelength. The gap distance between the bus waveguide and ring resonator is 75 nm

inside the ring as a function of gap distance. Based on the results, it is clear that the most effective gap distance is 160 nm.

Figure (4.4) shows the transmission spectrum on the output 1 port for signal, pump, and idler waves where the gap distance is 160 nm. Furthermore, the FSR for each peak is highlighted in the figure, with an approximate value of 5 nm. This value is in good agreement with the initial assumption.

The properties resonance peaks of the micro ring resonator are characterized by fitting a Lorentzian function that is given by

$$f(\lambda) = -A\frac{1}{1+\left[\frac{c}{\gamma}\left(\frac{1}{\lambda}-\frac{1}{\lambda_{\text{res}}}\right)\right]^2} + B\left(\frac{c}{\lambda}\right) \tag{4.12}$$

where γ is half width at half maximum. The Lorentzian fitting method is a commonly used method to investigate resonance characteristics. It is quite reliable and robust method for extracting parameters such as FWHM, which is essential for finding the quality factor of the resonator that reveals its performance.

In Figure (4.5), the Lorentzian fitting to the resonance peak at the pump wavelength (782 nm) is shown. The full width at half maximum (FWHM) is measured to be 0.0061. Using the equation (4.5), the quality factor of the silicon nitride ring resonator with 10 μm radius, 460 nm height, and 570 nm width is calculated to be approximately

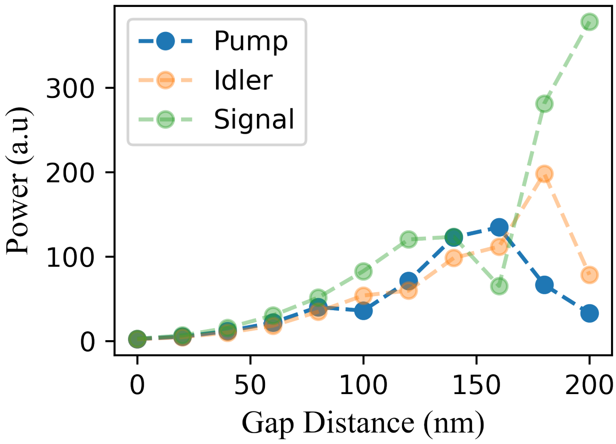

Figure 4.3. Power coupling from the bus waveguide to ring resonator with 460 nm height and 570 nm width as a function of gap distance between bus waveguide and ring resonator

$Q = 1.2 \times 10^5$. Moreover, positioning the 2D plane power monitor beneath the microring resonator device unveils whispery gallery modes, demonstrating the occurrence of total internal reflection within the resonator, as shown in Figure (4.6).

In the table (4.1), Q-factors in the literature for the $\mathrm{Si_3N_4}$ waveguide using a pump wavelength near 780 nm are shown. Compared to the values in the references, the simulation used in the thesis for the ring resonator gives promising results.

Table 4.1.: Q-factors in the literature for a Si_3N_4 ring resonator with a pump wavelength near 780 nm

Material	Wavelength(nm)	Diameter(μm)	Q-factor	Ref.
Si_3N_4	668.38	25	$(1.52 \pm 0.02) \times 10^5$	[5]
Si_3N_4	780	20	1.5×10^4	[41]
Si_3N_4	780	20	1.2×10^5	This Work
Si_3N_4	780	600	$(1.38 \pm 0.04) \times 10^6$	[42]
Si_xN_y	850	200	1.3×10^5	[43]
Si_3N_4	933.62	25	$(1.04 \pm 0.02) \times 10^6$	[5]

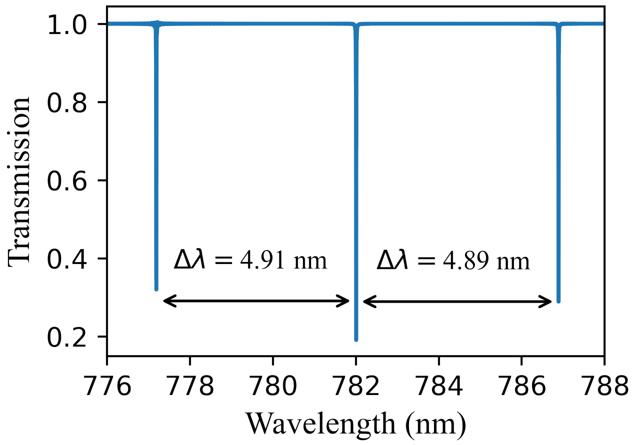

Figure 4.4. Transmission spectrum of a Si_3N_4 resonator with a 460 nm height and 570 nm width, and 10 μm radius from output 1 port as a function of wavelength. The gap distance between the bus waveguide and ring resonator is 160 nm, and the FSRs are 4.91 nm and 4.89 nm from signal to pump and pump to idler, respectively

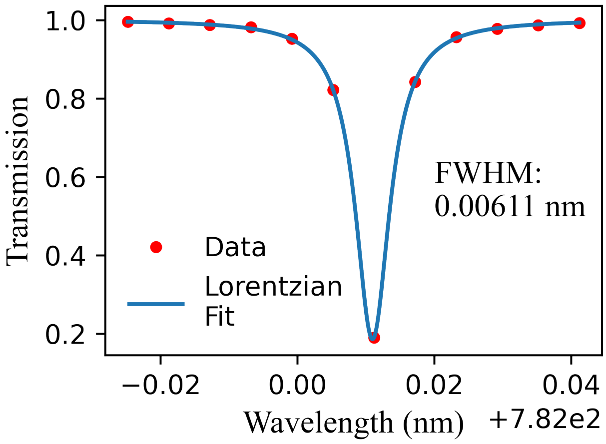

Figure 4.5. Lorentzian fitting to pump resonance peak of a Si_3N_4 resonator with a 460 nm height and 570 nm width, and a 10 μm radius. The gap distance between the bus waveguide and ring resonator is 160 nm, and FWHM is 0.0061 nm

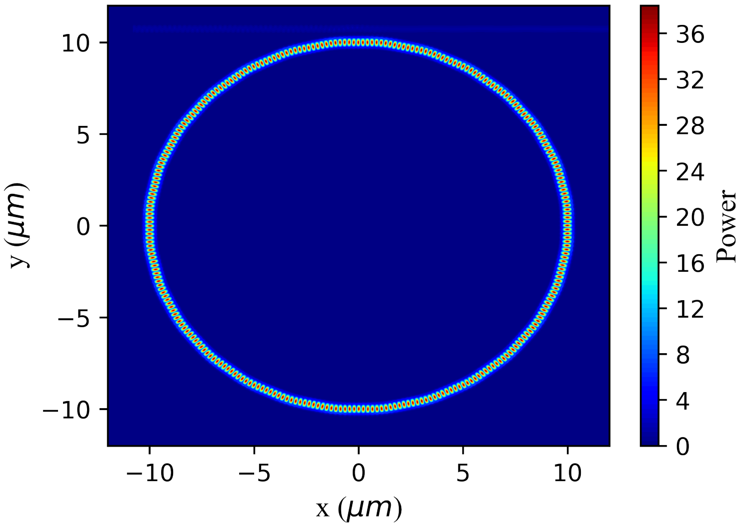

Figure 4.6. Whispering gallery modes of a Si_3N_4 resonator with a 460 nm height and 570 nm width and a 10 μm radius. The gap distance between the bus waveguide and ring resonator is 160 nm

4.2. Photon Pair Generation

FWM is a highly researched topic that utilizes a ring resonator to create large intensity through constructive interference inside the ring. Third-order nonlinear interaction is made possible by the elastic scattering of two photons at the pump frequency, resulting in the generation of two new photons at different frequencies[44] , known as the signal and idler. This study focuses on the design of ring resonators using classical electromagnetic modeling to investigate the nonlinear properties of Si_3N_4 material. It is expected to increase the efficiency of the ring resonator classically and enhance the quantum mechanical nonlinear interaction due to the connection between quantum mechanical and classical FWM efficiencies. The primary objective is to achieve spontaneous FWM since it results in the production of correlated[45] or entangled photons[46,47] for quantum information and quantum computation. Moroever, photon pair generation rate is given by[45,48,49]

$$R = (P\gamma)^2 4 \frac{Q^3 v_g^4}{\omega^3 L^2} \left(1 \pm \sqrt{\Gamma}\right)^3 \tag{4.13}$$

for continuous wave pump and signal and idler wave are generated at resonances of the ring resonator. In equation (4.13), P is the pump power, L is the ring length, Q is the quality factor, v_g is group velocity, γ is a nonlinear coefficient, and Γ is the normalized transmission through the waveguide. For the given ring resonator in Figure (4.6), the photon pair generation rate based on equation (4.13) is found to be approximately $6.5 \times 10^5 Hz$ for 1 mW pump and the losses are neglected.

CHAPTER 5

CONCLUSION

In this thesis, the design processes of strip waveguides and micro-ring resonators to produce photon pairs using nonlinear materials through the FWM in the visible spectrum range, focusing on the 780 nm pump wavelength, have been studied. Chapter 2 begins with an overview of the theoretical background of nonlinear optics and then focuses on new frequency generation through the FWM processes. Then, we discussed how to fulfill the phase and energy matching conditions under different scenarios based on the dispersion regimes of the waveguide. Chapter 2 also shows that employing appropriate dispersion engineering techniques makes it possible to achieve photon pair generation within a waveguide. In this context, it has been discussed that operating in an anomalous and near-zero dispersion regime can lead to the FWM process. In contrast, the strong anomalous regime can result in supercontinuum generation.

In Chapter 3, we introduced the different types of waveguides commonly used in literature. We focused on the strip waveguide to analyze its dispersion properties, as it serves as the basis for ring resonators and provides strong confinement. We also explored nonlinear materials and their applications in the literature. Based on our research, we selected the Si_3N_4 material due to its compatibility with CMOS technologies, low propagation loss, high refractive index contrast, and broad transparency window.

We then examined dispersion engineering on strip waveguides to determine the appropriate geometry, as tailoring dimensions is crucial for achieving phase-matching conditions. Consequently, we calculated the waveguide's width and height, effective refractive index, dispersion values, effective areas, and nonlinear coefficients. Utilizing this knowledge, we identified a smaller dimension range for further analysis.

Subsequently, we found that a waveguide with a height of 460 nm and a width of 570 nm met the criteria for zero dispersion wavelength and optimal field confinement. Additionally, we presented the mode profile of this waveguide geometry.

In Chapter 4, we focused on studying ring resonators with specific thickness and width based on dispersion studies. Our goal is to align the resonance peaks of ring resonators with the FWM. Initially, we demonstrated the fundamental properties of ring resonators and then determined the ring radius to be 10 μm in order to achieve a 5 nm FSR. We then conducted var-FDTD simulations, varying the distance between the bus waveguide and ring resonator, and found the optimal distance to be 160 nm. Finally, we demonstrated that using a Lorentzian fit to the resonance peak at 780 nm yielded an FWHM of 0.00611 nm. Utilizing these values, we calculated the Quality factor to be 1.2×10^5 and the photon pair generation rate to be 6.5×10^5, which is comparable to values found in the literature.

REFERENCES

1. Philipp, H. R. Optical Properties of Silicon Nitride. *Journal of The Electrochemical Society* **1973**, *120*, 295.
2. Gisin, N.; Thew, R. Quantum communication. *Nature Photonics* **2007**, *1*, 165–171.
3. Monroe, C. Quantum information processing with atoms and photons. *Nature* **2002**, *416*, 238–246.
4. O'Brien, J. L.; Furusawa, A.; Vučković, J. Photonic quantum technologies. *Nat. Photonics* **2009**, *3*, 687–695.
5. Lu, X.; Li, Q.; Westly, D. A.; Moille, G.; Singh, A.; Anant, V.; Srinivasan, K. Chip-integrated visibleâtelecom entangled photon pair source for quantum communication. *Nature Physics* **2019**, *15*, 373–381.
6. Dudley, J. M.; Genty, G.; Coen, S. Supercontinuum generation in photonic crystal fiber. *Rev. Mod. Phys.* **2006**, *78*, 1135–1184.
7. Moille, G.; Li, Q.; Lu, X.; Srinivasan, K. PyLLE: A fast and user friendly lugiato-lefever equation solver. *J. Res. Natl. Inst. Stand. Technol.* **2019**, *124*, 1–13.
8. Lin, Q.; Agrawal, G. P. Silicon waveguides for creating quantum-correlated photon pairs. *Opt. Lett.* **2006**, *31*, 3140–3142.
9. Sharping, J. E.; Lee, K. F.; Foster, M. A.; Turner, A. C.; Schmidt, B. S.; Lipson, M.; Gaeta, A. L.; Kumar, P. Generation of correlated photons in nanoscale silicon waveguides. *Opt. Express* **2006**, *14*, 12388–12393.
10. Takesue, H.; Tokura, Y.; Fukuda, H.; Tsuchizawa, T.; Watanabe, T.; Yamada, K.; Itabashi, S.-i. Entanglement generation using silicon wire waveguide. *Applied Physics Letters* **2007**, *91*, 201108.
11. ichi Harada, K.; Takesue, H.; Fukuda, H.; Tsuchizawa, T.; Watanabe, T.; Yamada, K.; Tokura, Y.; ichi Itabashi, S. Generation of high-purity entangled photon pairs using silicon wire waveguide. *Opt. Express* **2008**, *16*, 20368–20373.
12. Takesue, H.; Fukuda, H.; Tsuchizawa, T.; Watanabe, T.; Yamada, K.; Tokura, Y.; ichi Itabashi, S. Generation of polarization entangled photon pairs using silicon wire waveguide. *Opt. Express* **2008**, *16*, 5721–5727.

13. Matsuda, N.; Jeannic, H. L.; Fukuda, H.; Tsuchizawa, T.; Munro, W. J.; Shimizu, K.; Yamada, K.; Tokura, Y.; Takesue, H. A monolithically integrated polarization entangled photon pair source on a silicon chip. *Scientific Reports* **2012**, *2*, 817.

14. Turner, A. C.; Foster, M. A.; Gaeta, A. L.; Lipson, M. Ultra-low power parametric frequency conversion in a silicon microring resonator. *Opt. Express* **2008**, *16*, 4881–4887.

15. Fukuda, H.; Yamada, K.; Shoji, T.; Takahashi, M.; Tsuchizawa, T.; Watanabe, T.; ichi Takahashi, J.; ichi Itabashi, S. Four-wave mixing in silicon wire waveguides. *Opt. Express* **2005**, *13*, 4629–4637.

16. Grassani, D.; Azzini, S.; Liscidini, M.; Galli, M.; Strain, M. J.; Sorel, M.; Sipe, J. E.; Bajoni, D. Micrometer-scale integrated silicon source of time-energy entangled photons. *Optica* **2015**, *2*, 88–94.

17. Hsieh, I.-W.; Chen, X.; Liu, X.; Dadap, J. I.; Panoiu, N. C.; Chou, C.-Y.; Xia, F.; Green, W. M.; Vlasov, Y. A.; Osgood, R. M. Supercontinuum generation in silicon photonic wires. *Opt. Express* **2007**, *15*, 15242–15249.

18. Bristow, A. D.; Rotenberg, N.; van Driel, H. M. Two-photon absorption and Kerr coefficients of silicon for 850â2200nm. *Applied Physics Letters* **2007**, *90*, 191104.

19. Dinu, M.; Quochi, F.; Garcia, H. Third-order nonlinearities in silicon at telecom wavelengths. *Applied Physics Letters* **2003**, *82*, 2954–2956.

20. Lamont, M. R.; Luther-Davies, B.; Choi, D.-Y.; Madden, S.; Eggleton, B. J. Supercontinuum generation in dispersion engineered highly nonlinear ($\gamma = 10$ /W/m) As2S3 chalcogenide planar waveguide. *Opt. Express* **2008**, *16*, 14938–14944.

21. Neo, R.; Schröder, J.; Paquot, Y.; Choi, D.-Y.; Madden, S.; Luther-Davies, B.; Eggleton, B. J. Phase-sensitive amplification of light in a $\chi(3)$ photonic chip using a dispersion engineered chalcogenide ridge waveguide. *Opt. Express* **2013**, *21*, 7926–7933.

22. Lamont, M. R.; Luther-Davies, B.; Choi, D.-Y.; Madden, S.; Gai, X.; Eggleton, B. J. Net-gain from a parametric amplifier on a chalcogenide optical chip. *Opt. Express* **2008**, *16*, 20374–20381.

23. Lamont, M.; Ta'eed, V.; Moss, D.; Roelens, M.; Madden, S.; Luther-Davies, B.; Eggleton, B. J. Error-free wavelength conversion via cross phase modulation in As2S3 chalcogenide glass rib waveguides. LEOS 2007 - IEEE Lasers and Electro-Optics Society Annual Meeting Conference Proceedings. 2007; pp 23–24.

24. Luan, F.; Pelusi, M. D.; Lamont, M. R.; Choi, D.-Y.; Madden, S.; Luther-Davies, B.; Eggleton, B. J. Dispersion engineered As2S3 planar waveguides for broadband four-wave mixing based wavelength conversion of 40 Gb/s signals. *Opt. Express* **2009**, *17*, 3514–3520.

25. Apiratikul, P.; Wathen, J. J.; Porkolab, G. A.; Wang, B.; He, L.; Murphy, T. E.; Richardson, C. J. K. Enhanced continuous-wave four-wave mixing efficiency in non-linear AlGaAs waveguides. *Opt. Express* **2014**, *22*, 26814–26824.

26. Lacava, C.; Pusino, V.; Minzioni, P.; Sorel, M.; Cristiani, I. Nonlinear properties of AlGaAs waveguides in continuous wave operation regime. *Opt. Express* **2014**, *22*, 5291–5298.

27. Absil, P. P.; Hryniewicz, J. V.; Little, B. E.; Cho, P. S.; Wilson, R. A.; Joneckis, L. G.; Ho, P.-T. Wavelength conversion in GaAs micro-ring resonators. *Opt. Lett.* **2000**, *25*, 554–556.

28. Pu, M.; Ottaviano, L.; Semenova, E.; Oxenløwe, L. K.; Yvind, K. Ultra-Low Threshold Power On-Chip Optical Parametric Oscillation in AlGaAs-On-Insulator Microresonator. CLEO: 2015 Postdeadline Paper Digest. 2015; p JTh5A.9.

29. Bauters, J. F.; Heck, M. J. R.; John, D. D.; Barton, J. S.; Bruinink, C. M.; Leinse, A.; Heideman, R. G.; Blumenthal, D. J.; Bowers, J. E. Planar waveguides with less than 0.1 dB/m propagation loss fabricated with wafer bonding. *Opt. Express* **2011**, *19*, 24090–24101.

30. Spencer, D. T.; Bauters, J. F.; Heck, M. J. R.; Bowers, J. E. Integrated waveguide coupled Si3N4 resonators in the ultrahigh-Q regime. *Optica* **2014**, *1*, 153–157.

31. Levy, J. S.; Gondarenko, A.; Foster, M. A.; Turner-Foster, A. C.; Gaeta, A. L.; Lipson, M. CMOS-compatible multiple-wavelength oscillator for on-chip optical interconnects. *Nat. Photonics* **2010**, *4*, 37–40.

32. Ferdous, F.; Miao, H.; Leaird, D. E.; Srinivasan, K.; Wang, J.; Chen, L.; Varghese, L. T.; Weiner, A. M. Spectral line-by-line pulse shaping of on-chip microresonator frequency combs. *Nat. Photonics* **2011**, *5*, 770–776.

33. Herr, T.; Hartinger, K.; Riemensberger, J.; Wang, C. Y.; Gavartin, E.; Holzwarth, R.; Gorodetsky, M. L.; Kippenberg, T. J. Universal formation dynamics and noise of Kerr-frequency combs in microresonators. *Nat. Photonics* **2012**, *6*, 480–487.

34. Pasquazi, A.; Ahmad, R.; Rochette, M.; Lamont, M.; Little, B. E.; Chu, S. T.; Moran-

dotti, R.; Moss, D. J. All-optical wavelength conversion in an integrated ring resonator. *Opt. Express* **2010**, *18*, 3858–3863.

35. Duchesne, D.; Peccianti, M.; Lamont, M. R. E.; Ferrera, M.; Razzari, L.; Légaré, F.; Morandotti, R.; Chu, S.; Little, B. E.; Moss, D. J. Supercontinuum generation in a high index doped silica glass spiral waveguide. *Opt. Express* **2010**, *18*, 923–930.

36. Peccianti, M.; Pasquazi, A.; Park, Y.; Little, B. E.; Chu, S. T.; Moss, D. J.; Morandotti, R. Demonstration of a stable ultrafast laser based on a nonlinear microcavity. *Nat. Commun.* **2012**, *3*, 765.

37. Razzari, L.; Duchesne, D.; Ferrera, M.; Morandotti, R.; Chu, S.; Little, B. E.; Moss, D. J. CMOS-compatible integrated optical hyper-parametric oscillator. *Nat. Photonics* **2010**, *4*, 41–45.

38. Lavrinenko, A.; Lægsgaard, J.; Gregersen, N.; Schmidt, F.; Søndergaard, T. *Numerical Methods in Photonics*; Optical Sciences and Applications of Light; CRC Press, 2014.

39. Zhu, Z.; Brown, T. G. Full-vectorial finite-difference analysis of microstructured optical fibers. *Opt. Express* **2002**, *10*, 853–864.

40. Hammer, M.; Ivanova, A. Effective index approximations of photonic crystal slabs: a 2-to-1-D assessment. *Optical and quantum electronics* **2009**, *41*, 267–283, Open Access.

41. Doolin, C.; Doolin, P.; Lewis, B. C.; Davis, J. P. Refractometric sensing of Li salt with visible-light Si3N4 microdisk resonators. *Applied Physics Letters* **2015**, *106*, 081104.

42. Sinclair, M.; Gallacher, K.; Sorel, M.; Bayley, J. C.; McBrearty, E.; Millar, R. W.; Hild, S.; Paul, D. J. 1.4 million Q factor Si3N4 micro-ring resonator at 780 nm wavelength for chip-scale atomic systems. *Opt. Express* **2020**, *28*, 4010–4020.

43. Samusenko, A.; Gandolfi, D.; Pucker, G.; Chalyan, T.; Guider, R.; Ghulinyan, M.; Pavesi, L. A SiON Microring Resonator-Based Platform for Biosensing at 850 nm. *Journal of Lightwave Technology* **2016**, *34*, 969–977.

44. Chen, N.; Wang, Z.; Wu, J.; Li, H.; He, S.; Fan, Z.; Fan, Y.; Zhang, X.; Zhou, Q.; Xu, J. Pushing photon-pair generation rate in microresonators by Q factor manipulation. *Opt. Lett.* **2023**, *48*, 5355–5358.

45. Hemsley, E.; Bonneau, D.; Pelc, J.; Beausoleil, R.; OâBrien, J. L.; Thompson, M. G.

Photon pair generation in hydrogenated amorphous silicon microring resonators. *Scientific Reports* **2016**, *6*, 38908.

46. Rahmouni, A.; Wang, R.; Li, J.; Tang, X.; Gerrits, T.; Slattery, O.; Li, Q.; Ma, L. Entangled photon pair generation in an integrated SiC platform. *Light: Science & Applications* **2024**, *13*, 110.
47. Ono, T.; Tsujimoto, Y.; Wakui, K.; Fujiwara, M. Quantum interference of pulsed time-bin entanglement generated from silicon ring resonator. *Scientific Reports* **2024**, *14*, 1051.
48. Helt, L. G.; Yang, Z.; Liscidini, M.; Sipe, J. E. Spontaneous four-wave mixing in microring resonators. *Opt. Lett.* **2010**, *35*, 3006–3008.
49. Azzini, S.; Grassani, D.; Galli, M.; Andreani, L. C.; Sorel, M.; Strain, M. J.; Helt, L. G.; Sipe, J. E.; Liscidini, M.; Bajoni, D. From classical four-wave mixing to parametric fluorescence in silicon microring resonators. *Opt. Lett.* **2012**, *37*, 3807–3809.